SEISMIC STRATIGRAPHIC ANALYSIS USING MULTIPLE ATTRIBUTES - AN APPLICATION TO THE F3 BLOCK, OFFSHORE NETHERLANDS

by

EFKAN KABACA

BO ZHANG, COMMITTEE CHAIR
İBRAHİM ÇEMEN, COMMITTEE CO-CHAIR
MARCELLO MINZONI
TONY SMITHSON

A THESIS

Submitted in partial fulfillment of the requirements
for the degree of Master of Science
in the Department of Geological Sciences
in the Graduate School of
The University of Alabama

TUSCALOOSA, ALABAMA

2018

ABSTRACT

Seismic stratigraphy analyzes the geological concepts of stratigraphy by identifying the seismic reflection termination patterns that may record stratal terminations such as onlaps, downlaps, erosional truncations, and toplaps. It is a common tool in the assessment of source reservoir and seal rocks during petroleum system analysis in a basin. However, identifying the reflection termination patterns on seismic sections line-by-line is a time-consuming task. This study demonstrates a new workflow for picking sequence-bounding surfaces semi-automatically using seismic waveform, acoustic impedance, and porosity attributes.

During this study, the workflow started with a process of selecting seismic attributes, followed by a manual interpretation of sequence boundaries on key seismic lines. The key lines are treated as control points for the semi-automatic seismic interpretation. Finally, the sequence boundaries are semi-automatically picked by finding the shortest path defined by multiple seismic attributes. To test the effectiveness of this workflow, I used a 3D seismic data set acquired over the Dutch sector of the North Sea. The workflow successfully traced the sequence boundaries between manually interpreted horizons.

DEDICATION

This thesis is dedicated to my family and girlfriend for their patience and endless support along the way.

LIST OF ABBREVIATIONS AND SYMBOLS

2D	Two Dimensional
3D	Three Dimensional
API	American Petroleum Institute
BSFR	Basal Surface of Forced Regression
CC	Correlative Conformity
CDP	Common Depth Point
CG	Central Graben
E	East
FSST	Falling Stage Systems Tracts
g/cm^3	Gram per cubic centimeter
GR	Gamma-ray
HST	High Stand Systems Tracts
km	Kilometer
LST	Low Stand Systems Tracts
m	Meter
MFS	Maximum Flooding Surface
mi	Mile
MRS	Maximum Regressive Surface
ms	Millisecond

m/s	Meter per Second
N	North
NM	Middle North Sea Group
NU	Upper North Sea Group
PNN	Probabilistic Neural Network
P-wave	Primary wave
RMS	Root Mean Square
SB	Sequence Boundary
SSTVD	Subsea Total Vertical Depth
s	Second
SU	Subaerial Unconformity
TST	Transgressive Systems Tracts
TWT	Two Way Travel Time
UTM	Universal Transverse Mercator
VG	Viking Graben
W	West
∞	Infinity

ACKNOWLEDGEMENTS

I would like to express the deepest appreciation to my advisor, Dr. Bo Zhang, and co-advisor, Dr. İbrahim Çemen, for their encouragement and endless patience throughout this study. This thesis would not have been possible without their valuable guidance and encouragement. I would also like to express my gratitude to Dr. İbrahim Çemen for the chance to study at the University of Alabama. I especially thank the other members of my thesis committee, Dr. Marcello Minzoni and Mr. Tony Smithson, who have willingly shared their precious time and influenced my thinking during the review process.

I am grateful to my family members Nizamettin Kabaca, Sevda Kabaca, Burak Kabaca, and my girlfriend Gözde Seviner for their patience throughout my research. I thank my friends Naihao Liu and Hao Wu for their help and for openly sharing ideas. Special thanks to all faculty and staff in the Department of Geological Sciences at the University of Alabama.

I am sincerely grateful to the Turkish Petroleum Corporation (TPAO) for financial aid of this program and all their support. Finally, I acknowledge the Netherlands Organization for Applied Scientific Research for releasing to the public all the data and information related to this research.

CONTENTS

LIST OF FIGURES

1. INTRODUCTION

Seismic stratigraphic analysis is based on identification and correlation of the sequence-bounding surfaces on seismic reflection profiles. This process is a time-consuming and tedious task that involves identification of individual boundaries on 2D seismic profiles and their correlation with each other to produce 3D sequence models. To reduce the interpretation time, various automatic horizon-picking algorithms are used in the practice of surface picking, which are generally based on a single seismic attribute such as dip or unwrapped seismic phases. However, neither the dip nor the seismic phases are usually accurate near faults and unconformity zones.

Seismic attributes are routinely used by geophysicist to assist seismic stratigraphic analyses. Barnes (2000) employed instantaneous seismic attributes to quantify seismic stratigraphic facies parameters. Randen et al., (1998) introduced a new technique that detects intersections of bedding configurations in seismic reflection profiles using seismic attributes. These intersections are believed to record stratal terminations such as onlaps, downlaps, erosional truncations, and toplaps. Gutiérrez (2001) improved the sequence stratigraphic interpretation of a fluvial system by using seismic inversion of 3D seismic data. Barrash and Reboulet (2004) used porosity data to investigate stratigraphic units. Contreras and Latimer (2010) used acoustic impedance as an additional attribute for sequence stratigraphy. Van Hoek et al. (2010) used geometric seismic attributes in seismic stratigraphic analysis. Khalifa and Alta'ee (2011) obtained the stacking of parasequences based on variations in porosity. Miller et al.

(2013) proposed that sequence-bounding unconformities are linked with abrupt changing surfaces of acoustic impedance.

In past decades, several methods have been proposed for picking horizons automatically. Maroni et al. (2001) introduced an automatic horizon-picking algorithm to map sediment layers on subbottom profiles. Their method is based on multi-resolution analysis through the wavelet transform which decomposes a signal into different scale components. Faraklioti and Petrou (2004) presented an automatic picking algorithm based on a surface detection technique. They used voxel connectivity method which relates voxels to their neighbors. They first identified small horizon fragments using connected component analysis. They then combined the fragments according to their orientation similarity to form horizons across the whole seismic survey. Yu et al. (2011) introduced a method for horizon picking using a pattern recognition algorithm, which can effectively pick a coherent horizon in 3D seismic data. Their method uses an orientation vector field (OVF of Yu et al., 2011) to select a pick within a trace to preserve the lateral continuity among seismic traces. They used the minimum-spanning tree algorithm (MST of Boruvka, 1926; Nesetril et al., 2001) to select the optimized traces. The method can reduce the interpretation time and improve the quality for automatic horizon picking. Wu and Hale (2015) used user-predefined seeds to semi-automatically pick the horizons. Their method is limited to the accuracy of the structure tensor computation.

This study aims to bring new insights into the following research questions:

(1) Is it possible to use seismic attributes to semi-automatically pick sequence-bounding surfaces? If yes, which seismic attributes should be used?

(2) Can semi-automatic horizon picking save time for seismic interpreter?

The goal of this study is to propagate the manual interpretation on interpreted lines to the whole seismic survey with the aid of porosity, acoustic impedance, and seismic waveform attributes. In this study, I developed a semi-automatic surface tracking algorithm to track the horizons. The algorithm is tested using a 3D seismic data set acquired in offshore Netherlands (Figure 1). The target zone of this study is the prograding units of the Eridanos delta. The picked horizons using the presented algorithm exactly follow the same phase of the seismic waveforms. The total interpretation time spent in the process of surface identification can be reduced by the new picking algorithm.

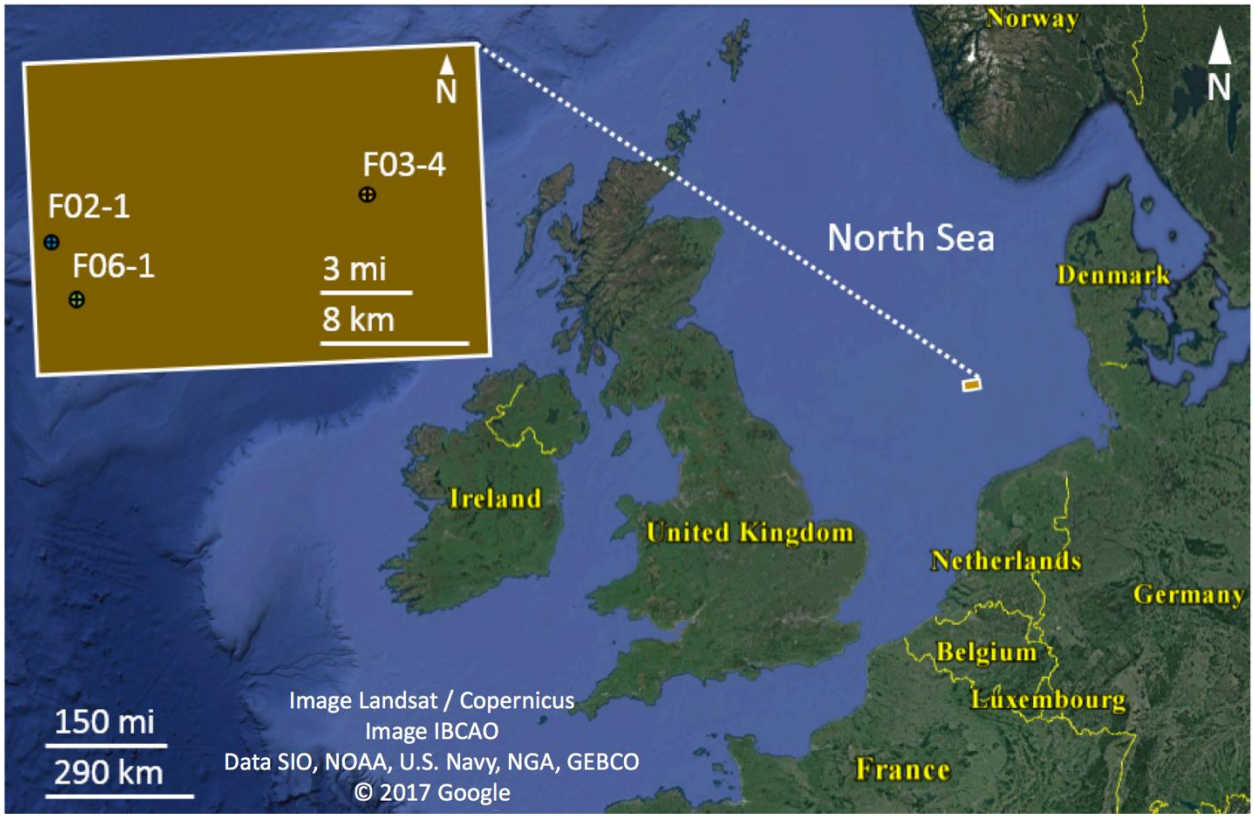

Figure 1. Location of the F3 Block and available wells overlaid on a Google Earth image.

2. GEOLOGIC OVERVIEW OF THE NORTH SEA REGION

2.1 Tectono-Stratigraphic Evolution

Geological history of the North Sea region includes four major tectonic phases (Cameron et al., 1992): (1) the Caledonian Orogeny Phase (Early Ordovician-Early Devonian), (2) the Variscan Orogeny Phase (Late Devonian-Late Permian), (3) the Kimmerian Orogeny Phase (Late Triassic-Early Cretaceous), and (4) the Alpine Orogeny Phase (Late Cretaceous-Present).

The geologic structures related to Caledonian Orogeny formed during the closure of the Iapetus Ocean when Baltica, Laurentia, and Avalonia plates collided from Early Ordovician to Early Devonian (Figure 2-A). During the Late Silurian, the North Sea region was dominated by a compressional regime due to the closure of Iapetus Ocean during the Caledonian Orogeny (Ziegler, 1975). Lower Paleozoic sediments metamorphosed during the Caledonian Orogeny to form the basement of the Southern North Sea (Cameron et al., 1993). Middle Devonian to Early Carboniferous siliciclastics and carbonates unconformably overlay the Caledonian basement (Wong et al., 2007).

The separation of peri-Gondwanan plates resulted in the development of the Rheic Ocean during the Ordovician along the southern flank of the Iapetus Ocean (Nance et al., 2012). The Variscan orogeny structures formed during the closure of the Rheic Ocean when the Laurussian and Gondwanan plates collided to form the supercontinent Pangaea, which took place from Late Devonian to Late Permian (Figure 2-B). In the Late Carboniferous Period, the southern North Sea became a foreland area of the south-west extended Variscan mountains. With the collapse

of the Variscan Mountains, its northern foreland was subjected to post-collisional extension. The extensional tectonics resulted in subsidence of east-west oriented northern and southern Permian Basins in the Variscan foreland basin. The creation of these basins are coeval post-Variscan events (Glennie, 1986). The northern and southern Permian Basins are separated by the Mid-North Sea High and Ringkøbing-Fyn High (Ziegler, 1977). The Netherlands are included in the southern Permian Basin (Geluk, 2017). Deltaic sedimentation prevailed during the late stages of the Variscan orogeny leading to the deposition of Upper Carboniferous coal measures, which formed the source rock for gas occurrences mainly in the southern North Sea (Ziegler, 1977). By the end of the Permian, the North Sea area was subjected to arid conditions, which resulted in the deposition of 1,000 m of Zechstein salt in the northern and southern Permian Basins (Ziegler, 1977).

During the Triassic, the region was covered by a widespread and shallow sea. The Mesozoic North Sea rift formed an integral part of the Arctic-North Atlantic rift system (Ziegler, 1977). The rifting started in the Late Triassic in the northern North Sea and spread southwards. The Permian framework was overprinted by a north-south trending rift system. In the Middle Jurassic, continued rifting lead to the development of the Viking Graben to the north and the Central Graben to the south.

During Oligocene-Miocene times, the Alpine orogeny and its compressional stresses caused reactivation of several basement faults and inversion of pre-Tertiary basins in the southern North Sea Basin (Figure 2-D). During the inversion, basement faults' reactivation in the southern North Sea triggered further halokinesis (Glennie and Boegner, 1981). The halokinesis generated intrusive salt structures such as stocks, diapirs, domes, and sills (Glennie, 2009). Rift system in the North Sea became inactive with the onset of sea-floor spreading in the Norwegian-

Greenland Sea. The North Sea Basin started to subside, and high sedimentation in the Tertiary caused accumulation of a 3,500-m thick succession in the Central North Sea (Ziegler, 1977). Tertiary and Quaternary deposits formed the Lower, Middle and Upper North Sea Groups (Figure 4), which together form the North Sea Supergroup (Wong et al., 2007).

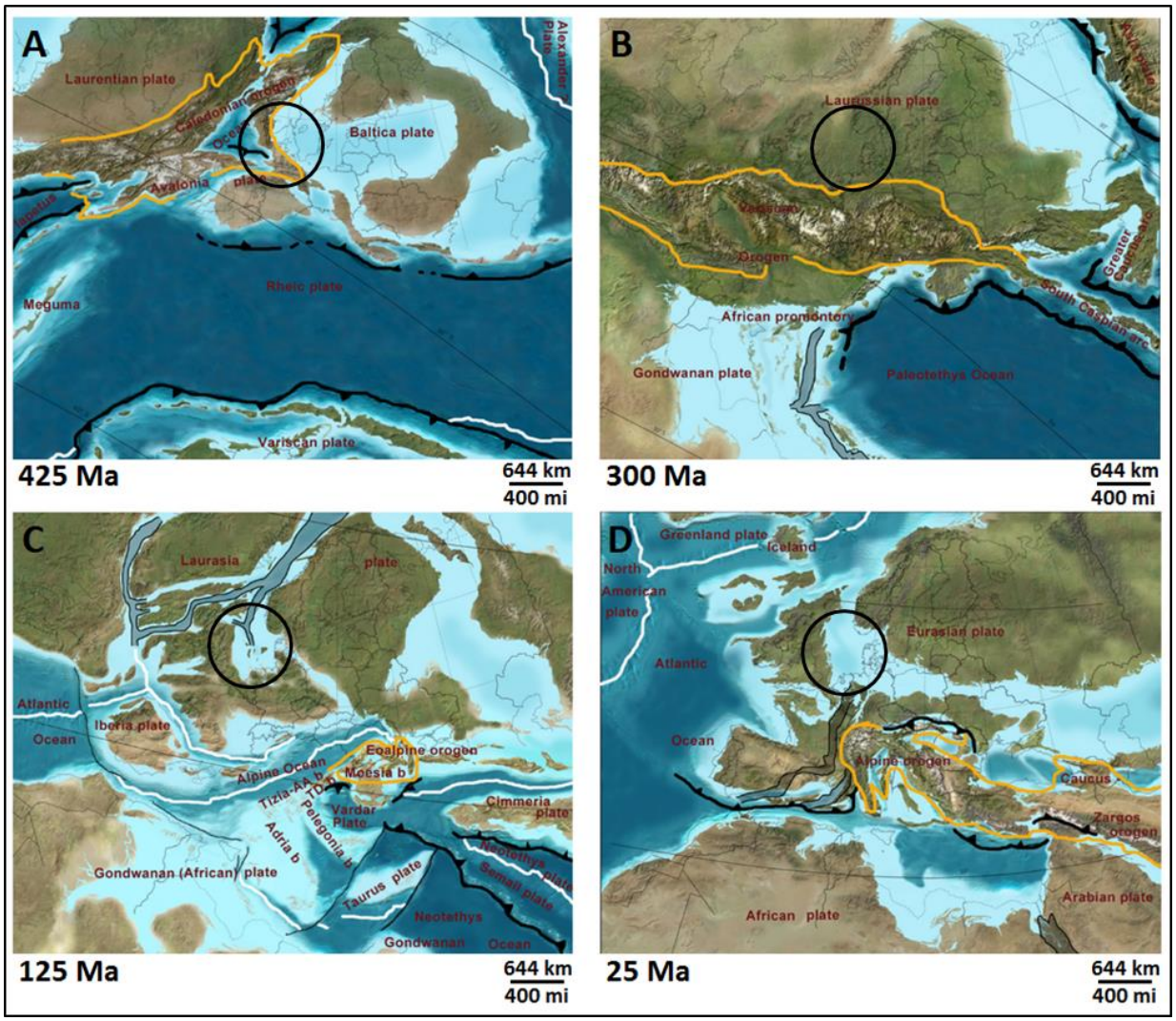

Figure 2. Paleogeographic maps showing the tectonic evolution of the North Sea region. (A) The Caledonian Orogeny phase, (B) the Variscan Orogeny phase, (C) the Kimmerian Orogeny phase, and (D) the Alpine Orogeny phase. Black circle indicates the position of the North Sea region (Modified from © Colorado Plateau Geosystems Inc.).

A combination of induced mantle convection and intraplate stresses resulted in domal uplift of the Fennoscandian Shield in the Oligocene time (Rohrman et al., 1995, 1996). Total uplift reached around 4,000–4,500 m in southern sectors of Norway (Riis, 1992, 1996; Sales, 1992; Lidmar-Bergström et al., 2000). During the Neogene, simultaneous uplift of the Fennoscandian Shield and subsidence in the Southern North Sea Basin resulted in the development of the Eridanos fluvial-deltaic system (Overeem et al., 2001; Figure 3). Sediments from Fennoscandian Shield in the north and the Variscan Massif to the south filled the Southern North Sea Basin and built an immense delta (Bijlsma, 1981). Differential loading throughout the region caused further movement of the Permian Zechstein salt. This remobilization strongly influenced all elements of the petroleum play in the North Sea region (Harding and Huuse, 2014).

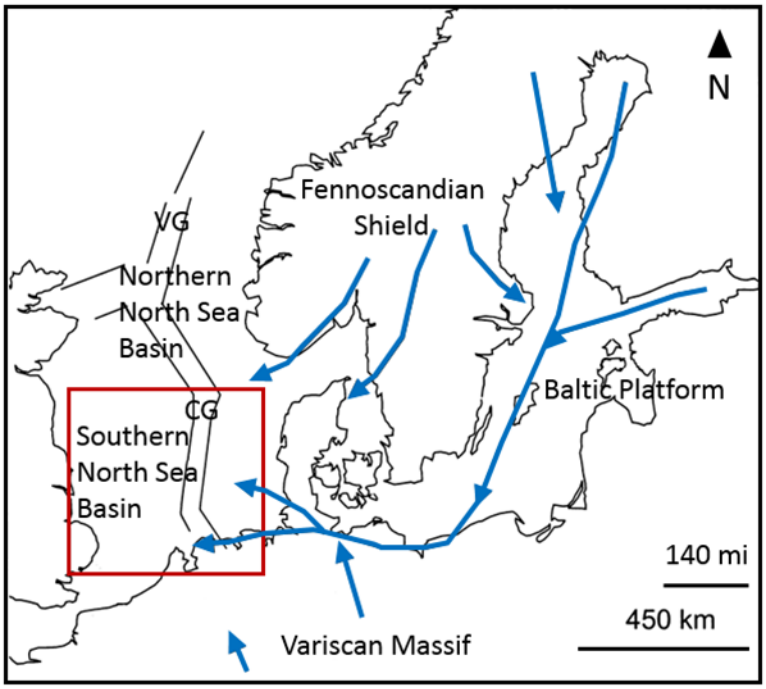

Figure 3. The Late Cenozoic Eridanos fluvial-deltaic system. VG: Viking Graben, CG: Central Graben (Modified from Overeem, 2001).

2.2 Stratigraphy

The stratigraphy of the survey area is recorded by the composite well log reports of the Wells F02-1, F06-1, and F03-4. Figure 4 shows nine main stratigraphic groups: (1) Zechstein Group (Late Permian), (2) Upper Germanic Trias Group (Middle-Late Triassic), (3) Schieland Group (Late Jurassic), (4) Scruff Group (Late Jurassic), (5) Rijnland Group (Early Cretaceous), (6) Chalk Group (Late Cretaceous), (7) Lower North Sea Group (Paleocene-Eocene), (8) Middle North Sea Group (Oligocene), and (9) Upper North Sea Group (Neogene-Quaternary). This study focuses on units comprising prograding deposits of the Eridanos delta of the Upper North Sea Group (Wolak et al., 2013).

The Upper North Sea Group (NU) unconformably overlies the Middle North Sea Group (NM) and records deposition from Neogene to Present. The NU consists of post-Oligocene shallow-marine sediments including clay, fine-to-coarse grained sand, local gravel, peat, and brown coal seams (Van Adrichem Boogaert, and Kouwe, 1993). The NU includes coarser sediments with more complex geometries compared to the underlying NM (Tetyukhina et al., 2010). The target interval of this study comprises three formations: (1) Breda Formation, (2) Kieseloolite Formation, and (3) Oosterhout Formation.

The Breda Formation consists of Miocene to earliest Pliocene age sediments deposited in a marginal marine environment. The formation comprises foreset and bottom-set sediments deposited in delta-front setting (Doppert et al., 1975). Lithologies include glauconitic sand, sandy clay, and clay. A glauconite-rich layer occurs commonly at the base, which is interpreted as a regional unconformity (Doppert et al., 1975).

The Kieseloolite Formation comprises Late Miocene, early Pliocene, and late Pliocene age sediments deposited in a river floodplain and coastal lowland (Van Adrichem Boogaert, and

Kouwe, 1993). The lower half of the formation is composed of coarse-grained clastics (sand and gravel), while the upper part consists of clay and sand (Van Adrichem Boogaert, and Kouwe, 1993). The lower portion of the Kieseloolite Formation merges into marine beds of the Breda Formation, and the upper portion merges into the Oosterhout Formation.

The Oosterhout Formation contains Pliocene to earliest Pleistocene sediments deposited in a shallow marine environment and in a delta-front setting. Lithologies include sand, sandy clay, and greenish clay. The Oosterhout Formation overlies the Breda Formation and intertongues with and is overlain by the deposits of Kieseloolite Formation, recording progradation (Doppert et al., 1975).

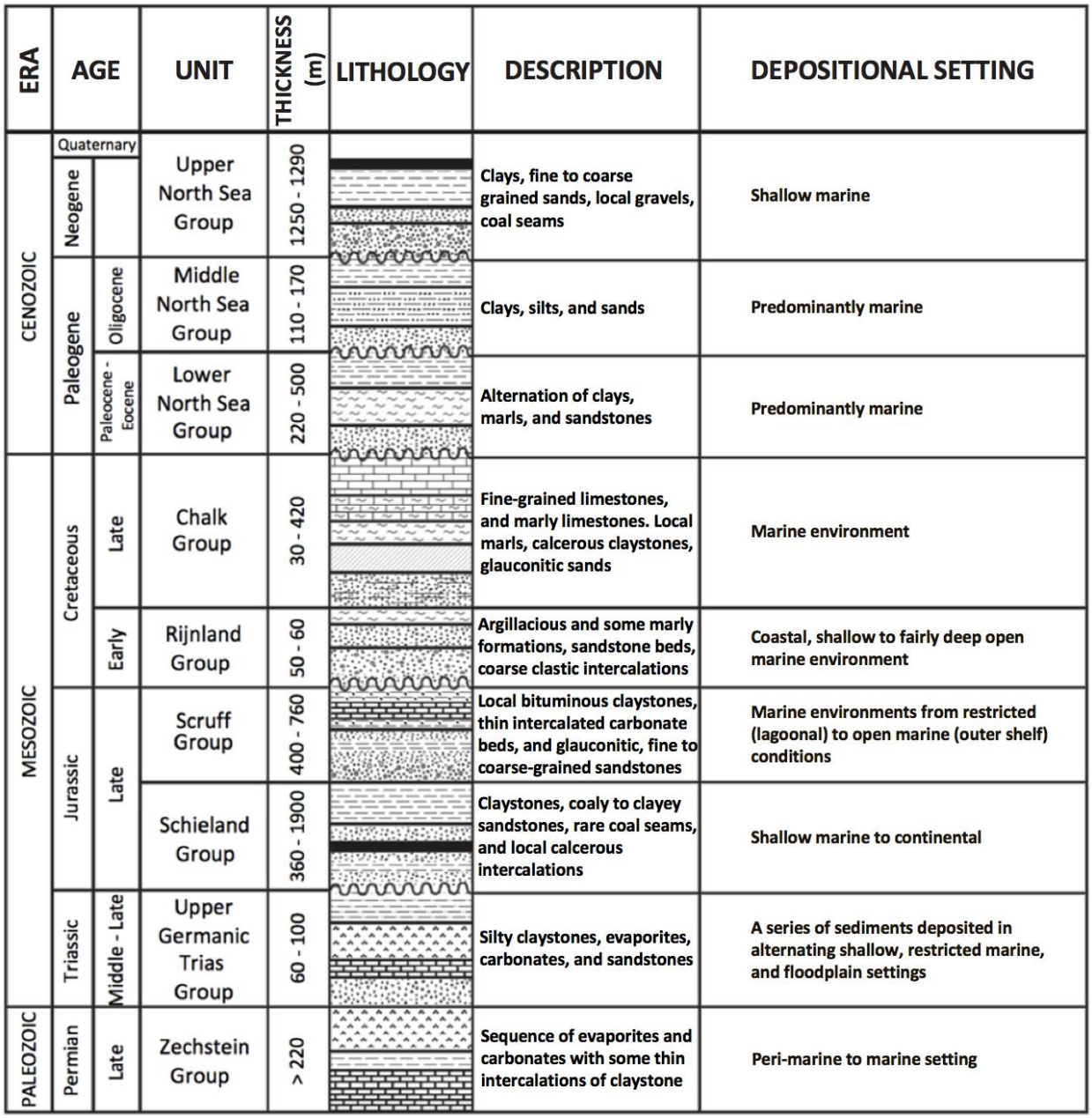

Figure 4. Generalized lithologic column of the survey area based on available well reports (www.nlog.nl).

3. DATA AND METHODOLOGY

3.1 Data Availability

Seismic data over the F3 Block (Dutch sector) of the North Sea were acquired in 1987 and consist of 651 inlines and 951 crosslines (Figure 5). The size of the survey area is 24 km in inline direction and 16 km in crossline direction with a 25 m x 25 m bin size. The two-way travel time record length of the seismic data is 1,848 ms with a sampling rate of 4 ms. Due to unavailability of the seismic data at the northeast corner of the survey area, only the first 501 of the 651 inlines were used in this study.

The data from three vertical wells in the study area were available for the study: F02-1, F06-1, and F03-4. Wells F02-1 and F03-4 were drilled in 1976 at X: 606549, Y: 6080124 and X: 623256, Y: 6082586 (UTM31), respectively. Well F06-1 was drilled in 1981 at X: 607902, Y: 6077213. Sonic and gamma-ray (GR) logs were available for all the wells. Density data were available only for Well F02-1. The density and sonic logs of Well F02-1 were used to train a neural network relationship between density and sonic logs. The trained neural network was then used to compute sonic logs for the Wells F06-1 and F03-4. Density porosity for all the wells was computed using sandstone matrix porosity formula:

$$\rho_{density} = \frac{\rho_{matrix} - \rho_{log}}{\rho_{matrix} - \rho_{fluid}} \quad (1)$$

Where $\rho_{density}$ is density porosity, ρ_{matrix} is matrix density (sandstone matrix, 2.65g/cm^3), ρ_{log} is measured bulk density, and ρ_{fluid} is mud-filtrate density (1.05 g/cm^3).

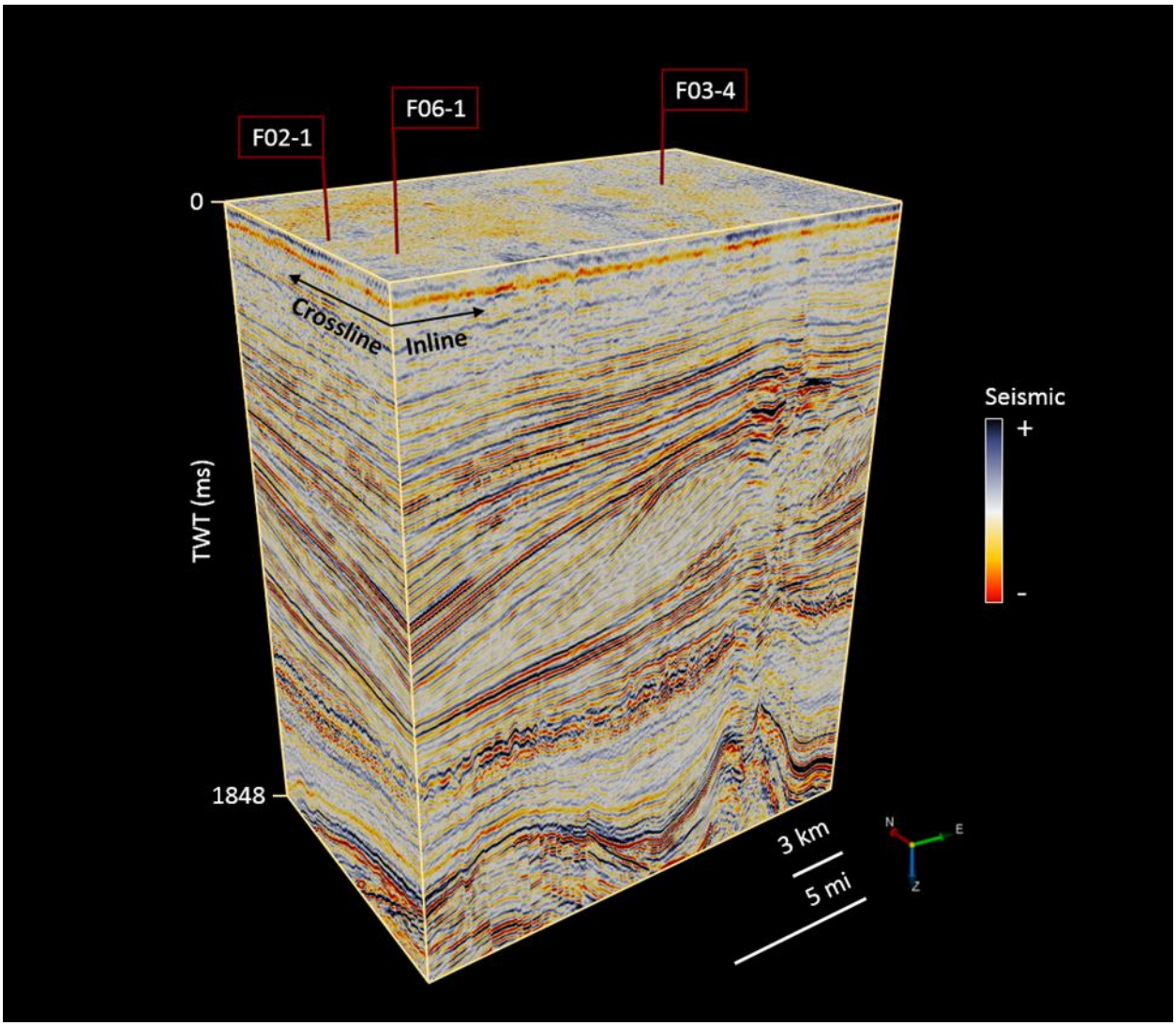

Figure 5. The 3D seismic volume with the locations of available wells.

3.2 Methodology

In this study, I applied a three-step workflow to semi-automatically identify sequence boundaries. The workflow starts with seismic attributions computation. Then, I manually identify the sequence boundaries on limited user-selected lines. Finally, I semi-automatically identify the sequence boundaries by using multiple seismic attributes analysis.

The selected seismic attributes used for sequence boundary identification include (1) seismic waveform, (2) P-impedance, and (3) porosity. I obtained the P-impedance through a model-based inversion and the porosity through a probabilistic neural network (PNN) analysis.

Stratigraphic analysis in this study comprises seismic sequence analysis and well-log sequence analysis. I interpreted seismic sequences and systems tracts using reflection patterns on limited seismic 2D sections. Then I calibrated my interpretation of sequence boundaries with well logs and semi-automatically propagated them through the seismic volume.

3.2.1 Seismic Attributes Computation

Seismic attributes are defined as any measurement extracted from seismic data (Taner et al., 1994). They provide some geological and geophysical information hidden in seismic images. The seismic attributes can measure time, amplitude, and attenuation of the seismic volume. In this study, I use original seismic waveform, P-impedance, and porosity as the inputs for semi-automatic horizon picking. These attributes were employed as they show sharp changes near sequence boundaries.

3.2.1.1 Acoustic Impedance Estimation

The acoustic impedance inversion includes transformation of seismic traces to a reflection coefficient series and then into acoustic impedance (Lindseth, 1979; Lavergne and Willm, 1977). This technique is the reverse of conventional forward modeling since it integrates

seismic and well log data to create a model of the earth (Russell, 1988). Latimer et al. (2000) pointed out the advantages of using impedance data versus conventional seismic data: "acoustic impedance is a rock property and a product of velocity and density. In contrast, seismic reflection is an interface property and a relative measurement of changes in acoustic impedance between layers. Having the data in layers, rather than at interfaces, improves visualization and vertical resolution. Also, the elimination of wavelet side-lobes and false stratigraphic-like effects makes sequence stratigraphic analysis easier."

The input of the seismic inversion process may be pre- or post-stack seismic reflection data. The basic theory behind all seismic inversion methods is found in the convolutional equation:

$$S = R * W + N \tag{2}$$

Where S is the seismic trace, R is the Earth's reflectivity, W is the band limited wavelet, and N is the additive noise. Noise is assumed to be random and uncorrelated with the signal. The label * denotes the convolution (Figure 6).

The reflectivity R is the contrast in acoustic impedance Z between the i^{th} and $(i+1)^{th}$ formations:

$$R_i = \frac{Z_{i+1} - Z_i}{Z_{i+1} + Z_i} \tag{3a}$$

$$Z_i = \rho_i \cdot v_i \tag{3b}$$

Where v_i and ρ_i are the P-wave velocity and density of the i^{th} layer, respectively.

Post-stack seismic inversion is a processing technique that aims to extract the acoustic impedance of the subsurface from surface measurements (stacked seismic data) (Russell and Hampson, 1991). The inputs of post-stack inversion usually include stacked seismic data, well

log data, and a set of geological constraints in the form of a model. The manner in which these inputs are combined depends on the inversion algorithms. Russell and Hampson (1991) described three post-stack seismic inversion methods: band-limited (BLI), sparse-spike (SSI),

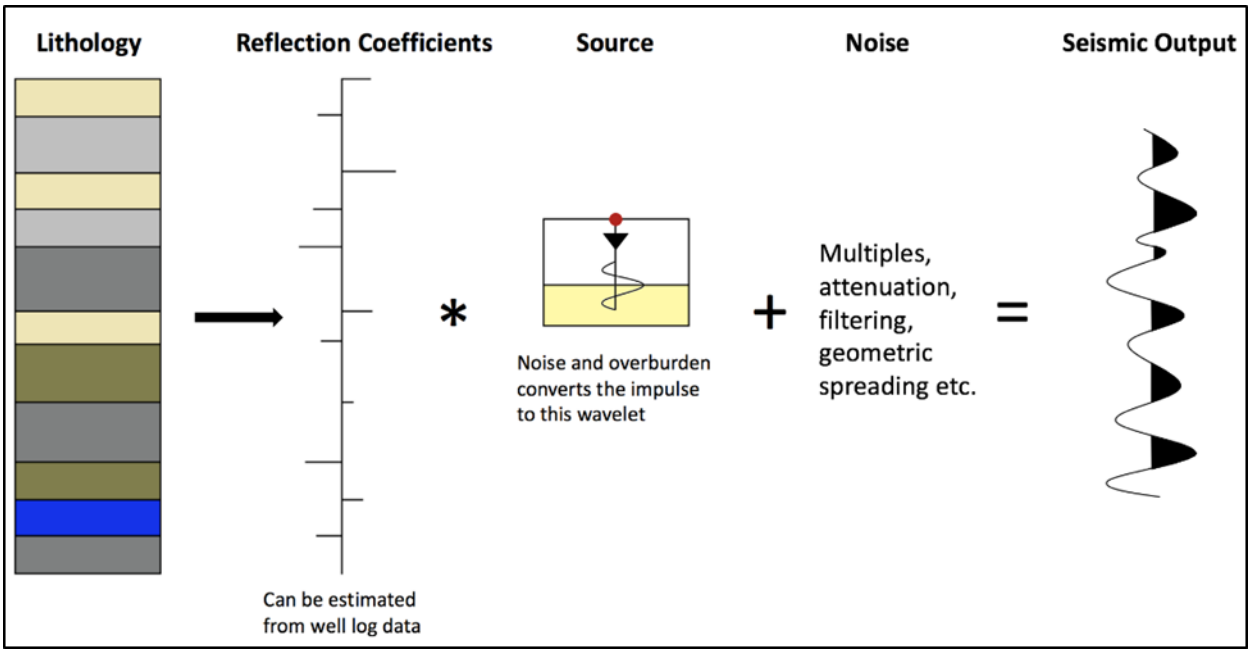

Figure 6. The convolutional theory. Reflection coefficient series are obtained from the impedance, which is the product of velocity and density. The seismic trace is the convolution between the Earth's reflectivity and a seismic source function (wavelet). (Modified from Walden and White, 1998).

and model-based (MBI) inversion. Band-limited inversion tends to produce limited frequency results. Sparse-spike inversion produces lower resolution models compare to model-based inversion. Model-based inversion produces the most robust results. Therefore, a model-based inversion approach was used to estimate P-impedance volumes.

The first step in the model-based inversion is building an initial impedance model of the earth. The initial model is then perturbed until the derived synthetic seismic best fits the real seismic data (Maurya and Sarkar, 2016; Figure 7). Some of the advantages of interpreting

seismic data in acoustic impedance rather than seismic amplitude domain can be summarized as (Maurya and Sarkar, 2016):

(1) Inversion increases the vertical resolution of seismic data by extending the frequency bandwidth. Increased resolution simplifies the stratigraphic definition.

(2) Acoustic impedance is a product of sonic velocity and bulk density; therefore, impedance results can be directly compared to well log measurements.

The MBI uses a generalized linear inversion (GLI) algorithm that assumes the seismic trace and the wavelet are known and modifies the initial model until the input seismic trace matches the synthetic trace (Cooke and Schneider, 1983). GLI produces a model that best fits the measured data using a least squares method. Figure 7 illustrates the workflow of post-stack seismic inversion. Inputs include post-stack seismic data, well logs, and geological constraints (interpreted horizons and faults). The output is the estimated P-impedance. Well log data and geological constraints are used to build the initial impedance model. GLI iterates updating the model parameters until the error between synthetic derived from P-impedance and seismic data is smaller than a user-defined threshold value. The mathematical expression of the GLI inversion can be expressed as (Russell, 1988):

$$F(M) = F(M_0) + \frac{\partial F(M_0)}{\partial M}\Delta M \tag{4}$$

Where F is modeling function, $F(M)$ is input seismic trace, M_0 is initial impedance model, $F(M_0)$ is synthetic seismic trace computed from the initial impedance model, M is true earth model, $\frac{\partial F(M_0)}{\partial M}$ is change in calculated values, ΔM is change in model parameters, and $\Delta F = F(M) - F(M_0)$ is error between the input seismic trace and the derived synthetic model trace.

In this study, I used the CGG Veritas Hampson-Russell software (HRS) package to obtain the P-impedance volume. The main steps in the model-based inversion procedure include (Maurya and Sarkar, 2016): (1) wavelet estimation and seismic well tie, (2) structure interpretation, (3) building background impedance model, (4) inversion analysis at well locations, and (5) applying results to the 3D seismic volume.

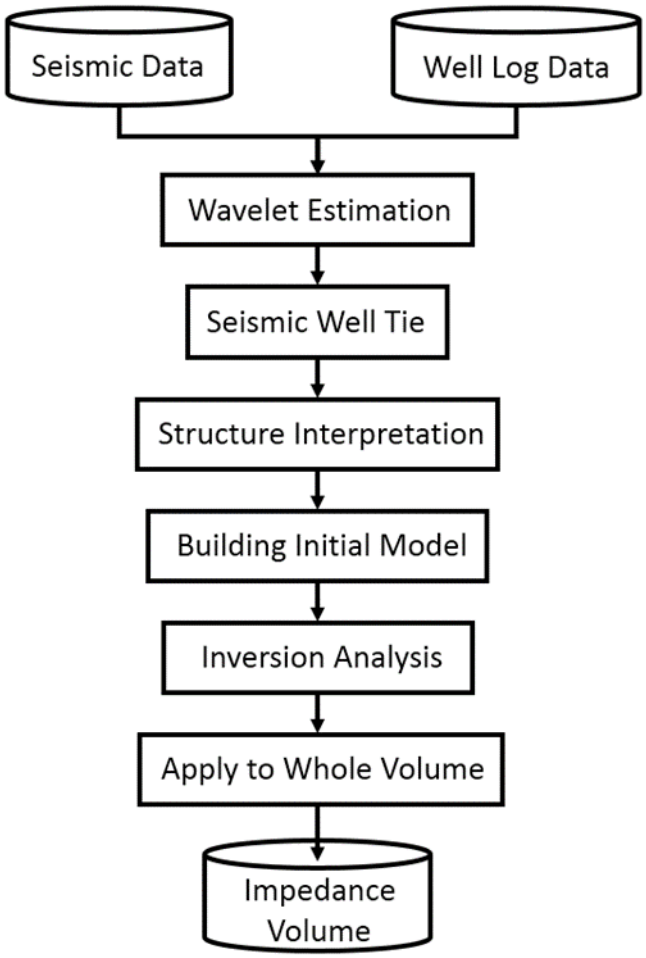

Figure 7. The workflow of model-based inversion (Modified from Maurya and Sarkar, 2016).

3.2.1.1.1 Wavelet Estimation and Seismic Well Tie

A seismic wavelet is the signature of the seismic source and the link between the seismic data (traces) and the geology (reflection coefficients) (Henry, 1997). Without knowing the wavelet, several valid interpretations of subsurface can be made (Henry, 1997). Therefore, wavelet extraction is perhaps the most important step in the seismic well tie, which is the correlation of a synthetic seismogram calculated from well log data with the seismic data. The synthetic seismogram is the convolution results between reflectivity derived from well logs and a wavelet. The purpose of seismic well tie is to integrate and calibrate information from well log data to the seismic section. The seismic well tie is the procedure of manually matching the synthetic seismic waveform and reflection seismic waveform. The seismic well tie process in Hampson-Russell software consists of the following steps:

1) extract a statistical zero-phase Ricker wavelet from the seismic data alone (Figure 8A),

2) stretch and squeeze the depth-time curve to correlate the synthetic with the seismic,

3) extract a new wavelet based on the correlated well and seismic data (Figure 8B),

4) repeat steps 2 and 3 until the difference between the seismic-well tie and wavelets of current and previous iterations falls within a user-defined threshold.

Figure 9 shows the results of a seismic well tie. The seismic well tie and wavelet estimation were performed for all the wells within the seismic survey. Each well has an optimum wavelet from the last seismic well tie loop. Usually, the optimum wavelets obtained for each well is unique. I obtained the final wavelets by averaging all the optimum wavelets.

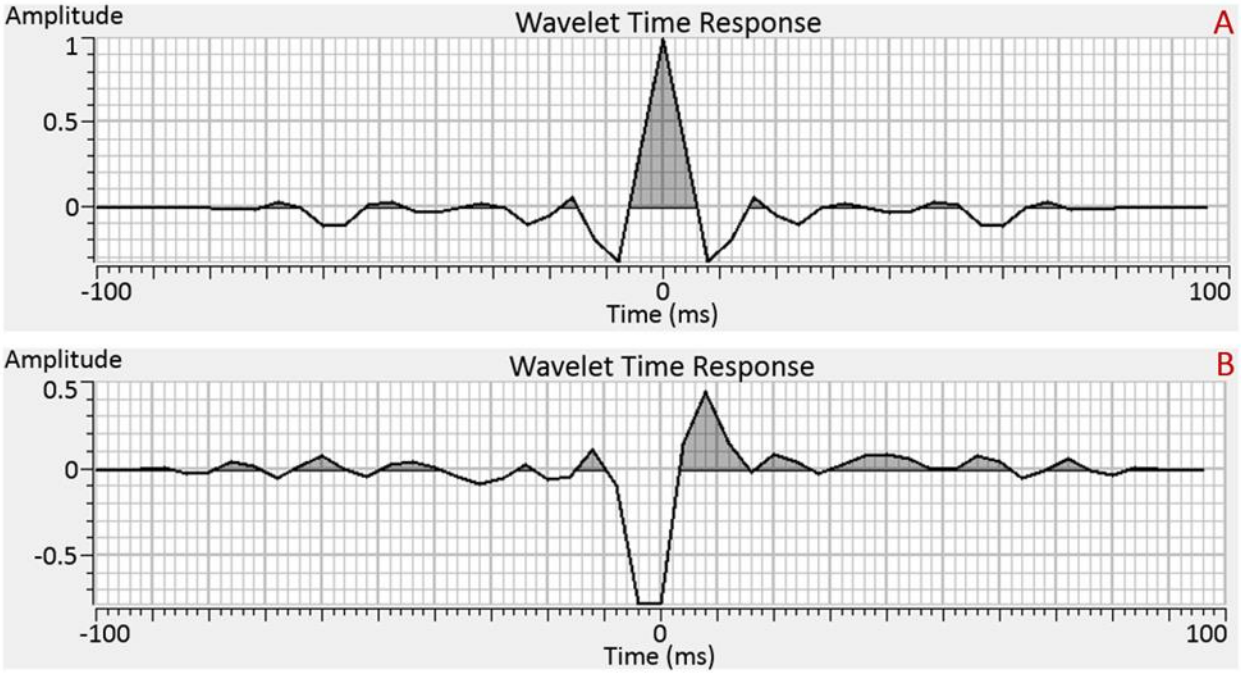

Figure 8. The seismic wavelet with (A) the statistical zero-phase Ricker wavelet, and (B) single average wavelet. The wavelets have a length of 200 ms.

3.2.1.1.2 Structure Interpretation

The model-based inversion requires a basic model of geologic interpretation after seismic well tie. Structure interpretation consists of manual interpretation of seismic events (horizons) on individual seismic profiles in both inline and crossline directions throughout the survey area. The interpreted horizons and well logs are then used to build the initial background model needed for the model-based inversion (Maurya and Sarkar, 2016).

Seismic survey of the F3 block reveals several geologic features such as truncated surfaces and folded/faulted structures caused by salt movement. These structures distort the lateral continuity of seismic reflections and make interpretation difficult. To better illustrate the configures of seismic reflections, I employed the instantaneous phase to facilitate the structure interpretation (Figure 11).

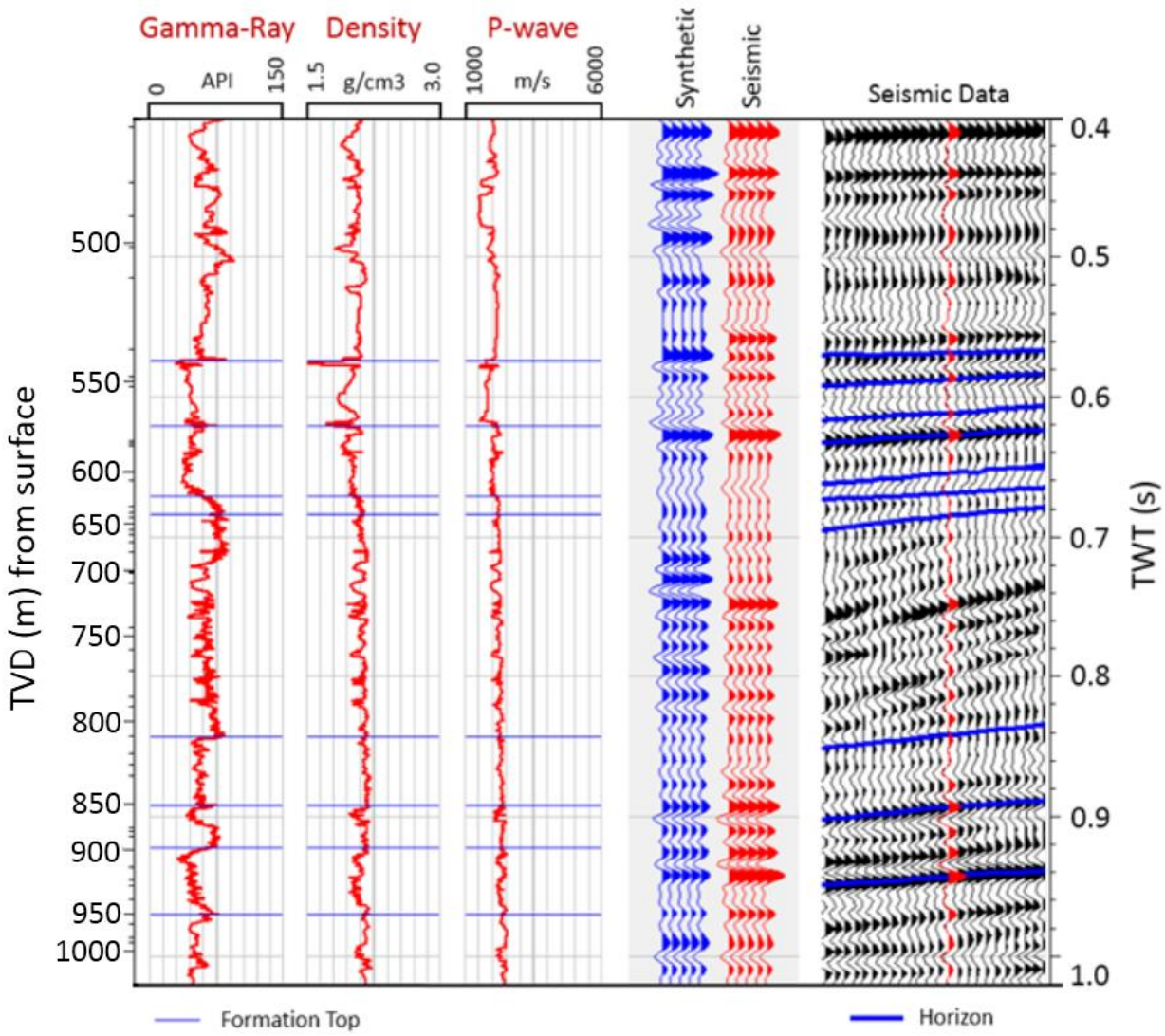

Figure 9. A seismic well tie using well log data and surface seismic data.

Instantaneous phase is a post-stack seismic attribute routinely used for lithologic and reservoir characterization (Taner et al., 2001). It is a good indicator of event continuity (Figure 10). Instantaneous phase is effective in showing faults, discontinuities, pinch-outs, and prograding geometries, which may otherwise be overlooked in the conventional seismic amplitude domain (Taner and Sheriff, 1977). It is computed using the components of the complex seismic trace, which are quadrature component (imaginary), and actual seismic trace

(real) (Taner et al., 1979). The instantaneous phase is defined by the equation:

$$\theta(t) = tan^{-1} f^*(t) / f(t) \quad (5)$$

Where $\theta(t)$ is instantaneous phase, $f^*(t)$ is the imaginary component of the complex seismic trace, and $f(t)$ is the actual seismic trace.

Based on the formation tops provided with the dataset and observed seismic reflection characteristics, I manually picked the candidate horizons (Figure 11).

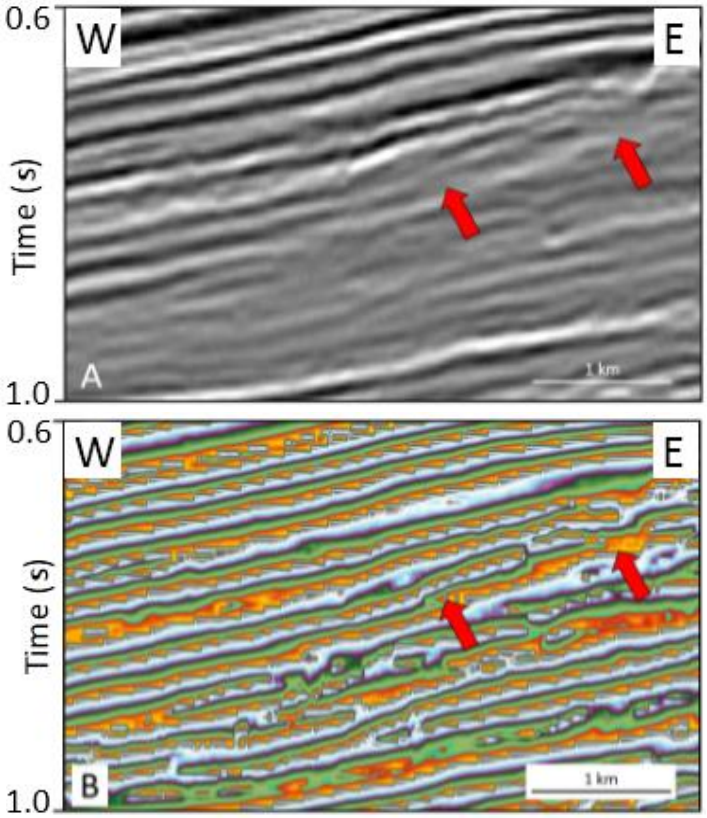

Figure 10. Comparison of two attributes. (A) Seismic amplitude, and (B) instantaneous phase. Arrows indicate an example seismic reflection that may be overlooked in seismic amplitude.

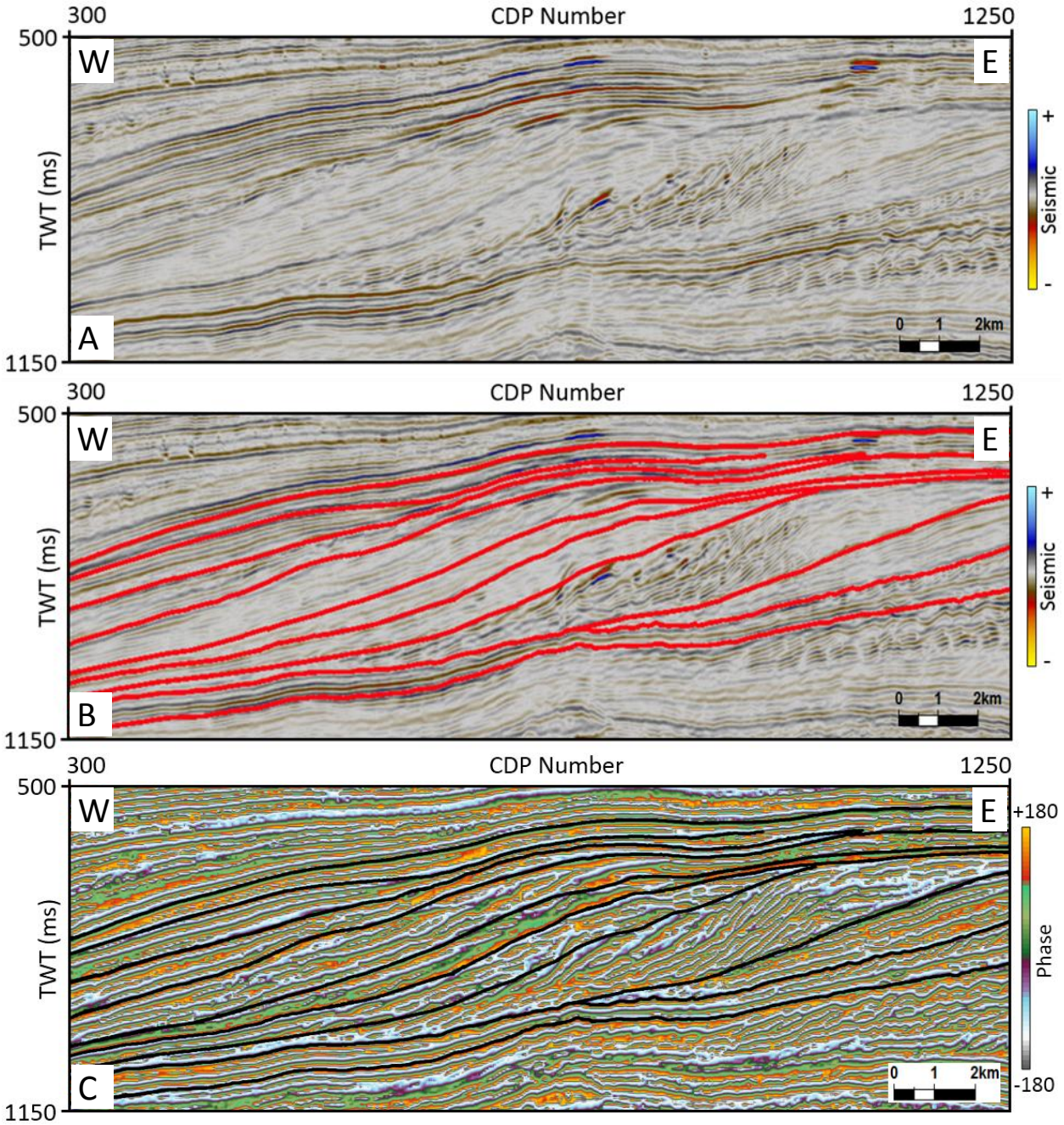

Figure 11. A representative inline seismic section with interpreted horizons. (A) Uninterpreted, (B) interpreted in original seismic waveform, (C) interpreted in instantaneous phase.

Figure 12 shows the initial low-frequency background model built from acoustic impedance logs and horizon interpretation. The model is low pass filtered as we desire to recover

missing low frequency content of seismic data from well log data.

Inversion analysis is performed by comparing the acoustic impedance log with the inverted acoustic impedance to set the inversion parameters at well locations. Figure 13 shows inversion analysis for the three wells within F3 block. Figure 13 shows the synthetic traces computed from the inverted acoustic impedance. Note that the correlation coefficient between the synthetic and the seismic trace is above 97% in all wells. The high correlation coefficient indicates that the inversion parameters can be confidently applied to the whole seismic volume. In terms of correlation coefficient between original and inverted acoustic impedance, there is no threshold and it is dependent on input data quality. Figure 14 shows the inverted P-impedance using model-based inversion. Note the improved vertical resolution when compared to the original seismic section shown in Figure 11.

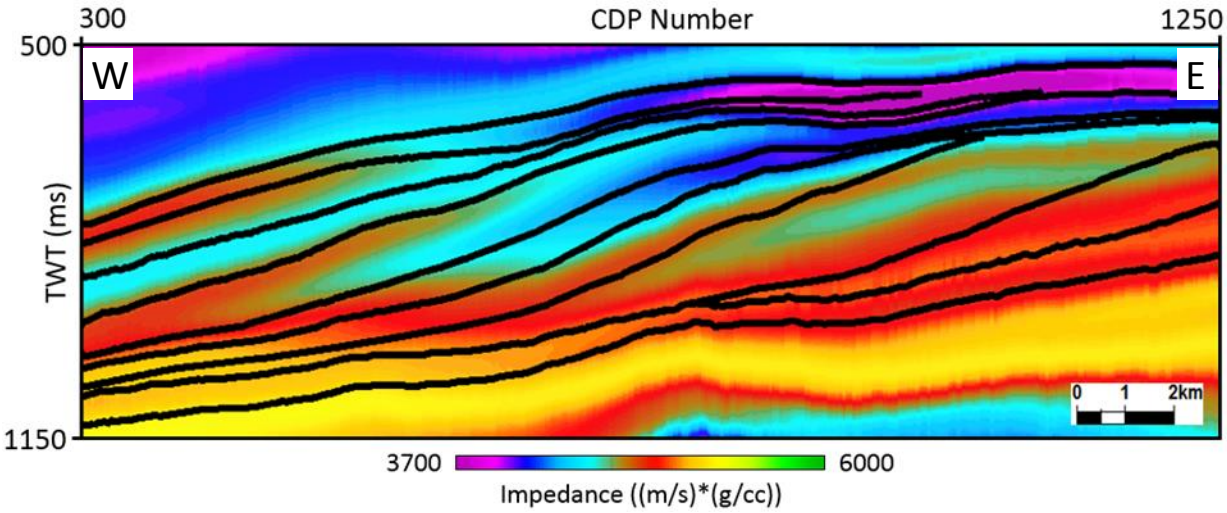

Figure 12. The initial impedance model used for the model-based inversion.

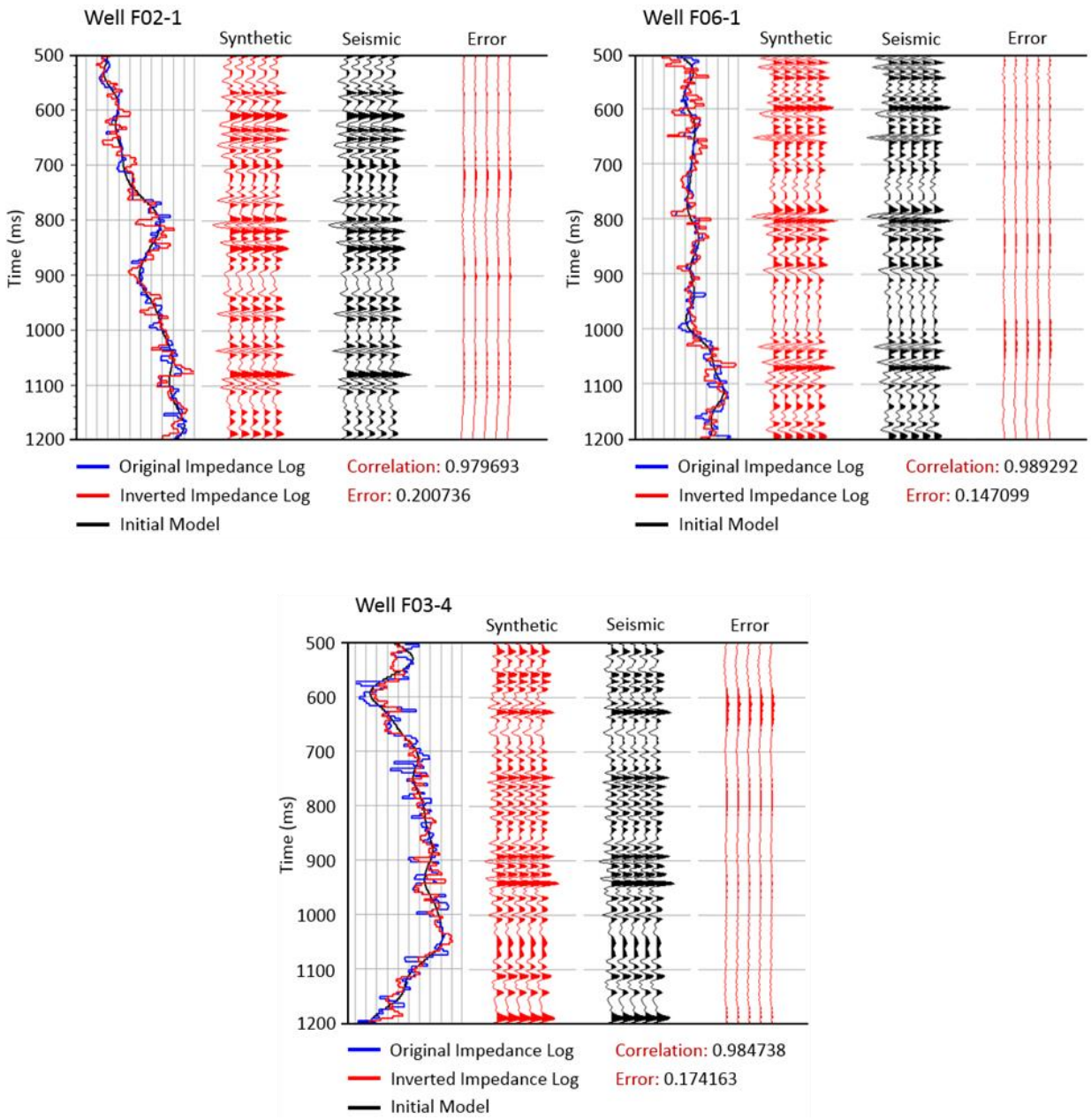

Figure 13. Inversion analysis results at well locations.

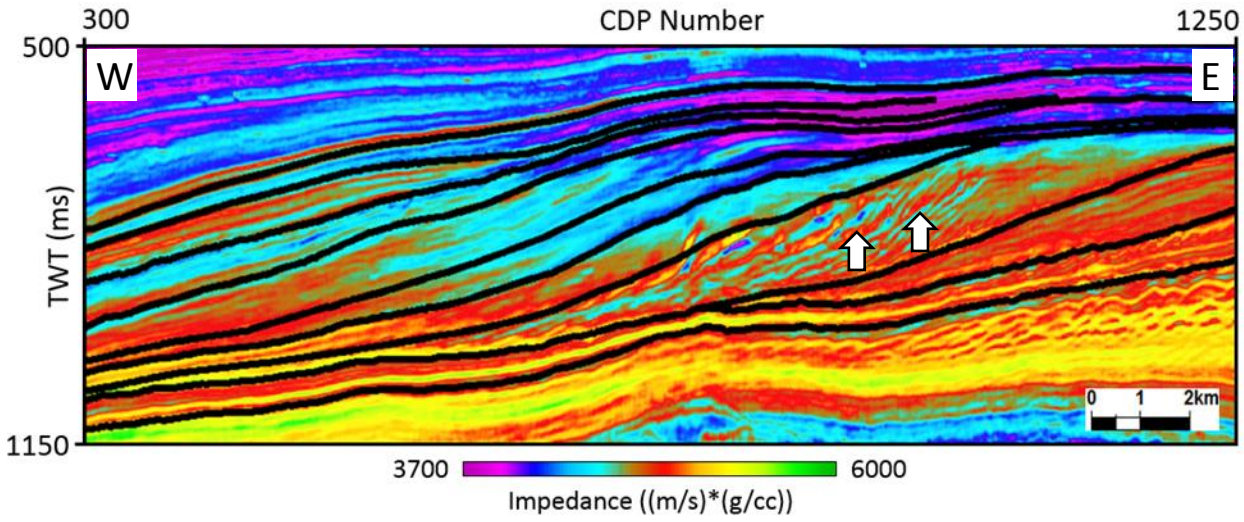

Figure 14. The inverted P-impedance with interpreted horizons (for white arrows, see chapter 5).

3.2.1.2 Porosity Volume Estimation

This section describes the porosity estimation from seismic data through neural network analysis. Schultz et al. (1994) proposed the use of multiple seismic attributes to predict porosity. I employed the Emerge package of HRS to estimate porosity (Figure 15). The objective is to derive a non-linear (neural network analysis) operator that can predict porosity from a set of selected seismic attributes. Firstly, an appropriate seismic attribute group is selected by stepwise regression analysis. Then, a neural network model is trained, validated, and tested to obtain mathematical relations between porosity and seismic attributes at well locations. Finally, the trained model is applied to the whole seismic to create a 3D porosity estimation.

3.2.1.2.1 Determining Seismic Attributes

Selecting proper seismic attributes is the most important step in the process of porosity estimation. A linear regression analysis is conventional cross-plotting between the candidate attributes and porosity logs to judge attributes individually according to their correlations with porosity logs:

$$y = a + bx \tag{6}$$

The coefficients "*a*" and "*b*" in the equation are derived through the least-square regression (Hampson et al., 2001):

$$E^2 = \frac{1}{N}\sum_{i=1}^{N}(y_i - a - by_i)^2 \tag{7}$$

Each attribute is ranked according to their correlations with porosity logs. To identify the best combination, Emerge uses a stepwise linear regression analysis (Draper and Smith, 1966).

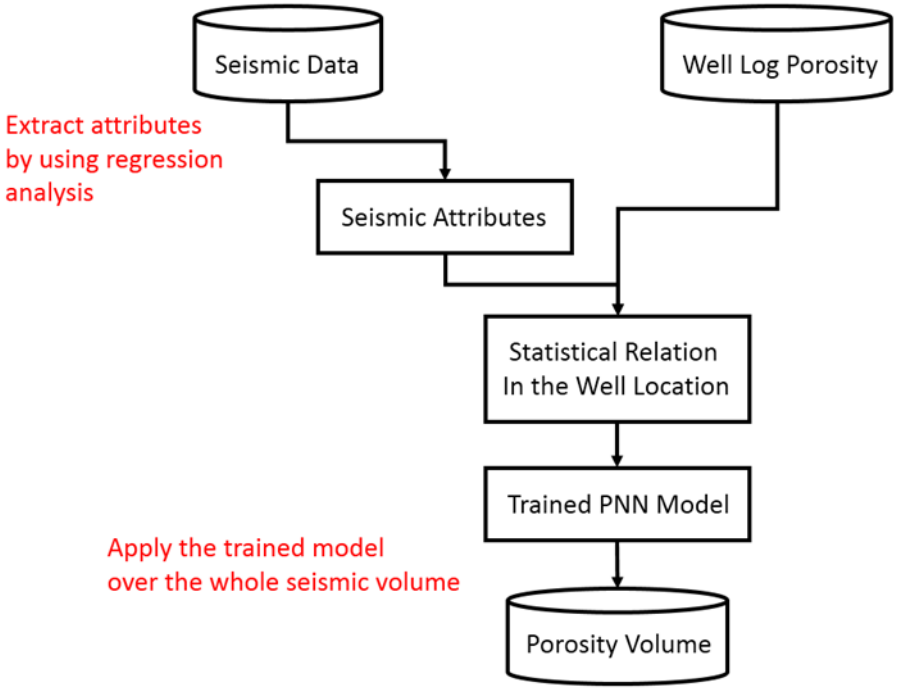

Figure 15. The workflow used in the porosity estimation (Modified from Hou et al., 2016).

The Stepwise analysis starts with choosing the highest ranked attribute as the best one. Then adds new seismic attributes one by one according to their ranks and performs linear regression analysis between multiple seismic attributes set and porosity log (Hampson et al., 2001):

$$L(t) = w_0 + w_1A_1(t) + w_2A_2(t) + w_3A_3(t) + \ldots \quad (8)$$

Where L is the porosity log, t is time, w is weight, and A is attribute (Figure 16). The weights are calculated through least-square optimization:

$$E^2 = \frac{1}{N}\sum_{i=1}^{N}(L_i - w_0 - w_1A_{1i} - w_2A_{2i} - w_3A_{3i})^2 \quad (9)$$

In theory, prediction error by using M+1 attributes is always less than or equal to that of using M attributes (Hampson et al., 2001). However, in practice, this is not always the case.

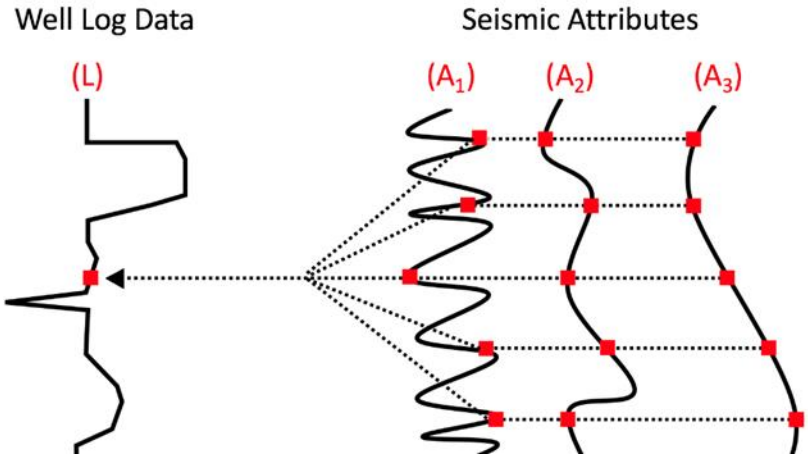

Figure 16. Prediction of the target well log data from a weighted group of seismic attributes. In the case of three attributes and five-point convolutional operator are used to estimate the value of one sample of porosity log (Modified from Hampson et al., 2001).

Sometimes adding new attributes to the regression decreases fit ("overtraining" of Kalkomey, 1997). Emerge uses a cross-validation technique which divides the data into two sets: (1) a validation data set and (2) a training dataset (Figure 17; Draper and Smith, 1966). The training set is used to derive the weight coefficients through least-square optimization, and the validation set is used to value the fitting degree trough cross-plotting. If the validation error curve gradually decreases and ends with the minimum, it is assumed that the number of attributes is optimum. If the validation error curve decreases and then starts to increase, the attributes are overtraining the

system. The training dataset consist of training samples from all wells, unless specified.

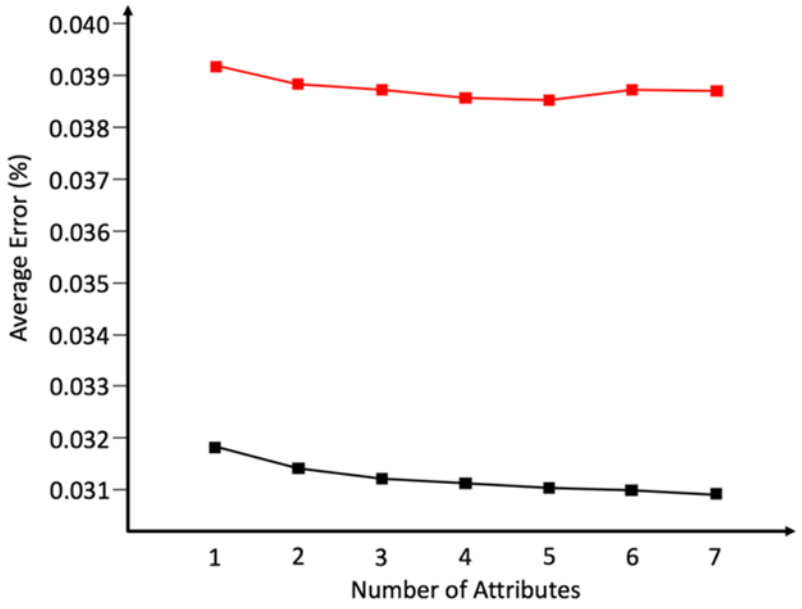

Figure 17. The results of the attributes training (black) and validation (red) procedure. The horizontal axis shows the number of attributes used in the prediction.

Figure 17 shows the error as a function of the number of attributes used in the linear regression. The black and red curves represent the training and validating data, respectively. Note that the average regression errors decrease with increasing attribute number. However, the average error increased after I included the sixth attribute (amplitude envelope) in the regression. This pattern shows that any additional attributes after the fifth attribute would overtrain the system and increase the validation error. Therefore, the best combination of attributes should contain the first five attributes in the multiple attributes list: (1) Seismic Inversion, (2) Filter 15/20-25/30, (3) Filter 5/10-15/20, (4) Instantaneous Phase, and (5) Amplitude Weighted Phase.

Typically, the well log data have higher frequency content than the seismic attributes. Therefore, correlating the well log data with seismic attributes sample-by-sample may not be the optimal choice (Hampson et al., 2000). A convolutional operator is recommended to overcome

the frequency incompatibility between the log data and the seismic attributes (Hampson et al., 2001). The convolutional operator relates a group of samples from seismic attributes to a single sample of the well log (Figure 16). The optimum operator length can be determined by using a testing tool provided in the Emerge software (Figure 18). The test suggests that a 1-point convolutional operator length has the minimum validation error of 0.038552 in porosity estimation when the selected five-attribute set is used.

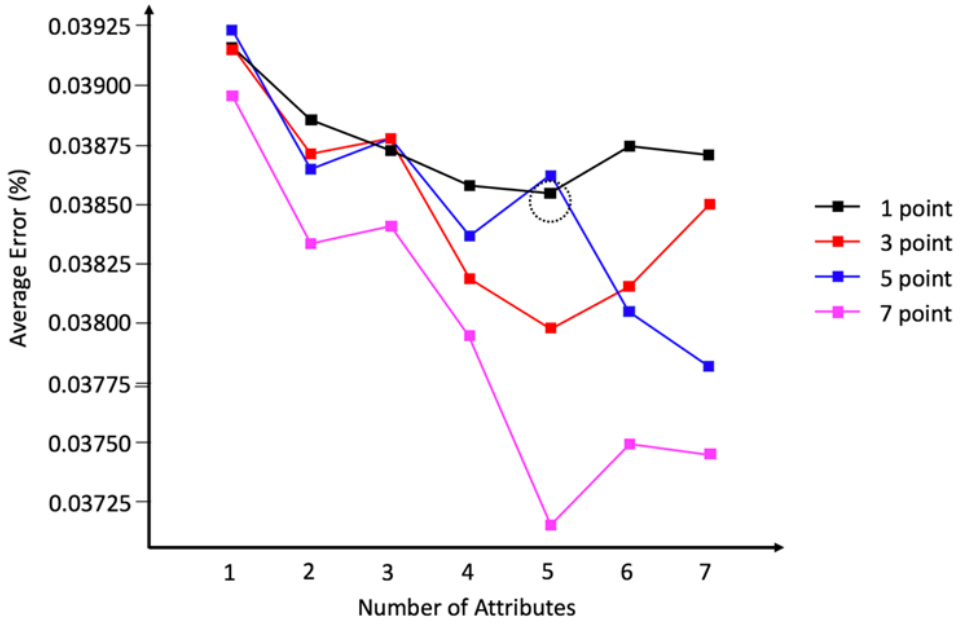

Figure 18. The results of determining the operator length. Five attributes with 1-point operator length has the lowest error value without overtraining the system.

3.2.1.2.2 Probabilistic Neural Network (PNN)

Figure 19-A shows limitations of the linear analysis that has been used so far. The graph shows log values cross-plotted against a single seismic attribute. The red line shows the linear regression through least–square optimization. Figure 19-B shows the relationship obtained through the PNN. It is clear that a higher order curve fits the data better.

Probabilistic neural networks (PNN; Specht, 1990) are powerful transform approaches

used to establish the mathematical relation between seismically derived attributes and porosity derived from an optimal training correlation (Chatterjee et al., 2016). In this study, I employed Hampson-Russell software to perform PNN analysis and obtained a mathematical mapping relationship between the selected seismic attributes and porosity.

After performing the PNN, the final correlation between predicted porosity and original well porosity is 0.878488, with a training error of 0.026742 %. Figure 20 shows a representative predicted porosity inline section.

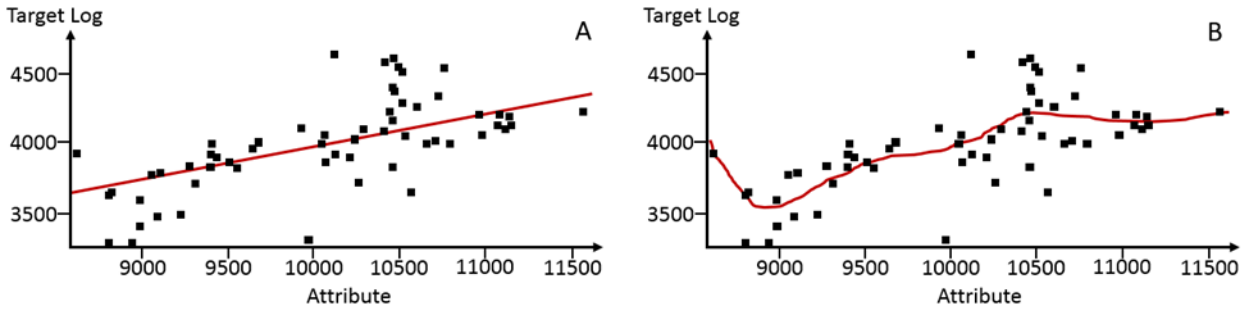

Figure 19. Cross plot of target log against seismic attribute using (A) the linear relationship regression, and (B) relationship obtained using PNN (Modified from Hampson et al., 2001).

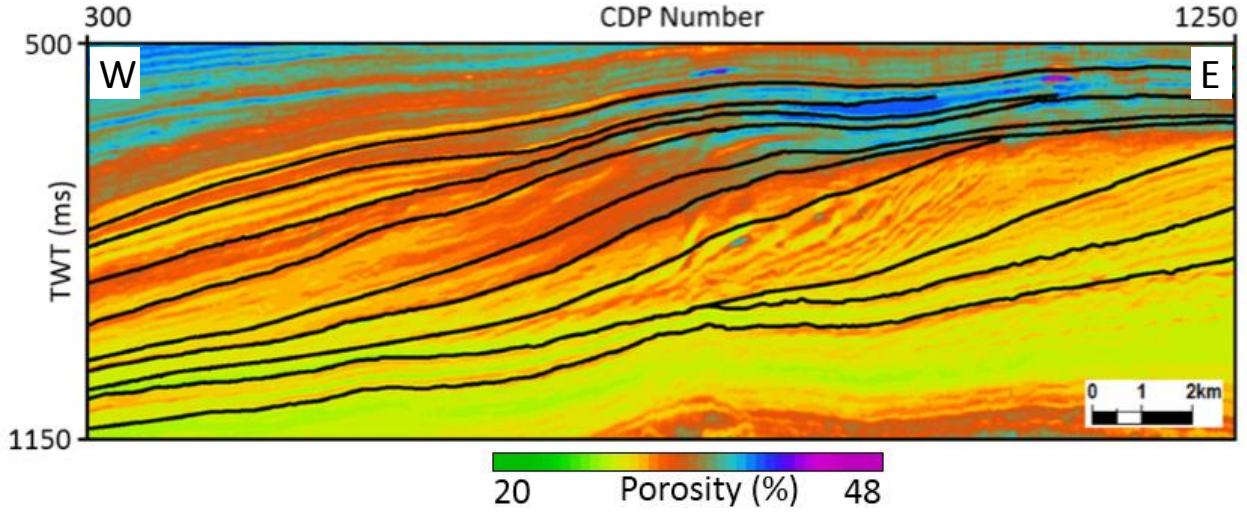

Figure 20. A representative estimated porosity inline section.

3.2.2 Seismic Stratigraphic Analysis

Seismic data provide lateral continuity and 3D insights for sequence stratigraphic interpretations. Seismic stratigraphic analysis techniques can provide some predictability to the distribution of facies through the application of sequence stratigraphic concepts (Vail, 1987). The fundamental unit of sequence stratigraphy is the sequence, which is a "relatively conformable succession of genetically related strata bounded at the top and base by unconformities or their correlative conformities (Mitchum et al., 1977)." A sequence is divided into systems tracts, which are defined by their position within the sequence and by the stacking pattern of parasequence sets.

Seismic sequence analysis defines seismic sequences and systems tracts by identifying discontinuities recorded in reflection termination patterns. The analysis starts with establishing geometric relationships of seismic reflections on seismic profiles. Aggradation, progradation, and retrogradation are the three general stacking patterns used to distinguish between different depositional systems (Figure 21). Sequence boundaries and other major surfaces are identified based on seismic reflection terminations such as onlap, downlap, toplap, and truncation (Figure 22). According to the reflection termination patterns, seismic reflections can be subdivided into systems tracts.

Well logs provide high resolution vertical stratigraphic data. Integration of seismic and well log data provides more accurate stratigraphic models of the sedimentary fill (Van Wagoner, 1991). The well log sequence analysis performed in this study is based on GR logs response from available wells. GR logs measure the radioactivity of rocks and are commonly used as a good proxy for grain size in siliciclatic systems (Van Wagoner, 1991). Abrupt changes in GR logs responses are commonly related to sharp lithological breaks associated with unconformities

and sequence boundaries (Krassay, 1998). Variation patterns of GR logs indicate changes in the

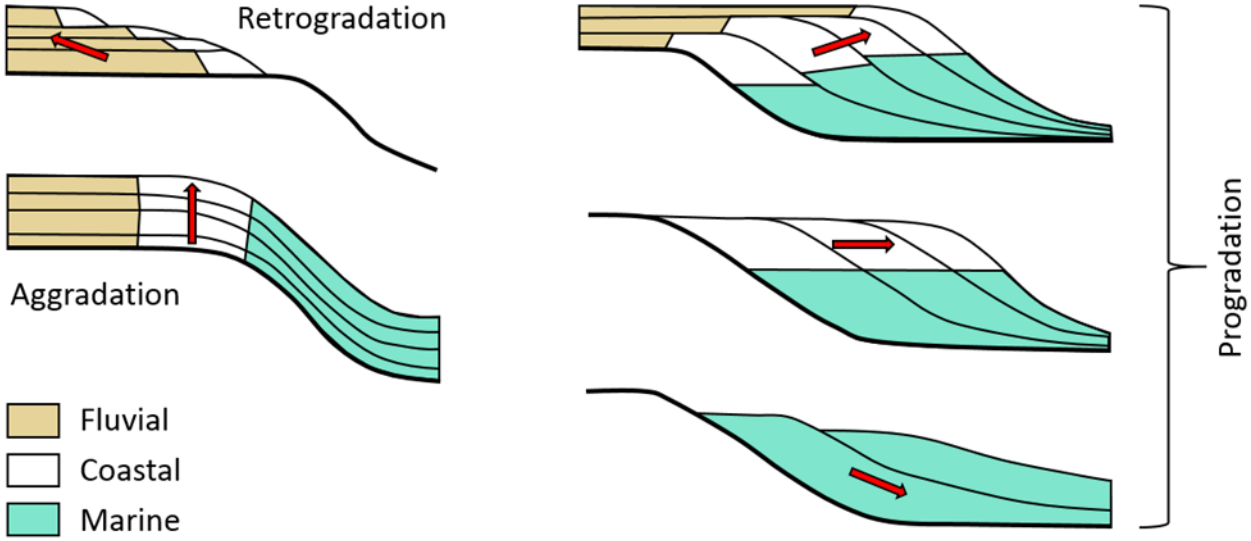

Figure 21. Retrogradational, aggradational, and progradational stratal stacking patterns (Modified from Martins-Neto and Catuneanu, 2010).

stacking patterns of sedimentary facies. GR log readings can be classified into upward decreasing, constant or upward increasing. The corresponding grain size changing patterns are interpreted as an upward increase, constant or upward decrease. “In deltaic systems, these patterns are commonly interpreted as prograding, aggrading, and retrograding systems, respectively.”

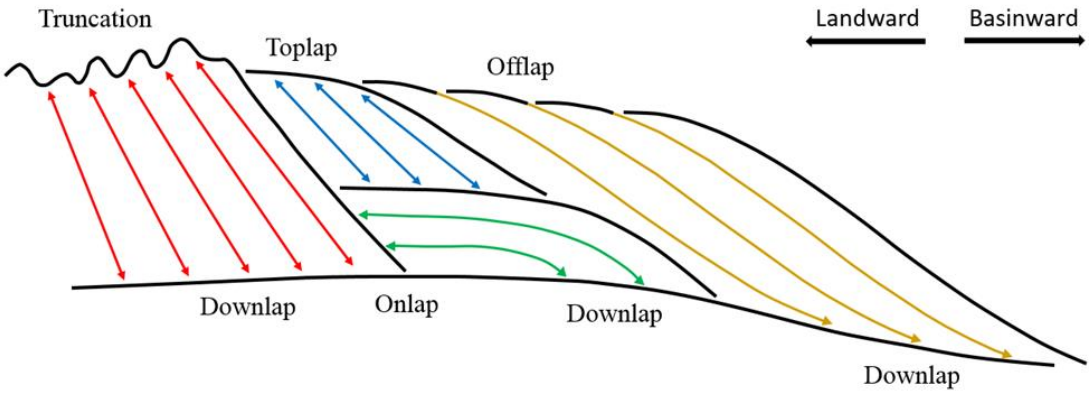

Figure 22. Geometric relationships (reflection terminations) associated with stratigraphic cycles (Modified from Catuneanu, 2006).

In this study, the sequence bounding surfaces have been identified based on reflection patterns on seismic lines, and the interpretation was then calibrated with GR logs. The sequence bounding surface interpretation was performed using the instantaneous phase attribute to highlight seismic reflection patterns (Figure 23). Depositional model IV (Hunt and Tucker, 1992; 1995), was followed during the analysis. This model consists of four systems tracts corresponding to the transgressive and regressive phases within one complete base-level cycle: transgressive systems tract (TST), highstand systems tract (HST), falling stage systems tract (FSST), and lowstand systems tract (LST). The sequence stratigraphic interpretation was performed on selected seismic sections, which are the inlines 100, 200, 300, 400, 500, and 600. The target zone of this analysis is basinward prograding sediments of the Eridanos delta. This interval contains siliciclastic shelf deposits comprising sand and shale (Overeem et al., 2001).

Following the interpretation of Quayyum et al. (2012, 2013), and Amosu and Sun (2017), three sequences were identified within the target interval by integrating seismic reflection terminations and GR log patterns. The lower sequence (Sequence 1) consists of TST, HST, and FSST. The intermediate sequence (Sequence 2) is comprised of LST, HST, and FSST, while the last sequence (Sequence 3) consists of LST, TST, and HST.

The basal unit of Sequence 1 consists of a set of parallel and landward restricted reflectors (Quayyum et al., 2013; Figure 25). The GR log for this interval shows an upward increasing trend ending with a peak in basinward wells (F02-1 and F06-1), while the trend is questionable in well F03-4. Ending peak was interpreted as a maximum flooding surface (Figure 24). Based on the reflection terminations and the GR response, this unit is interpreted as a TST.

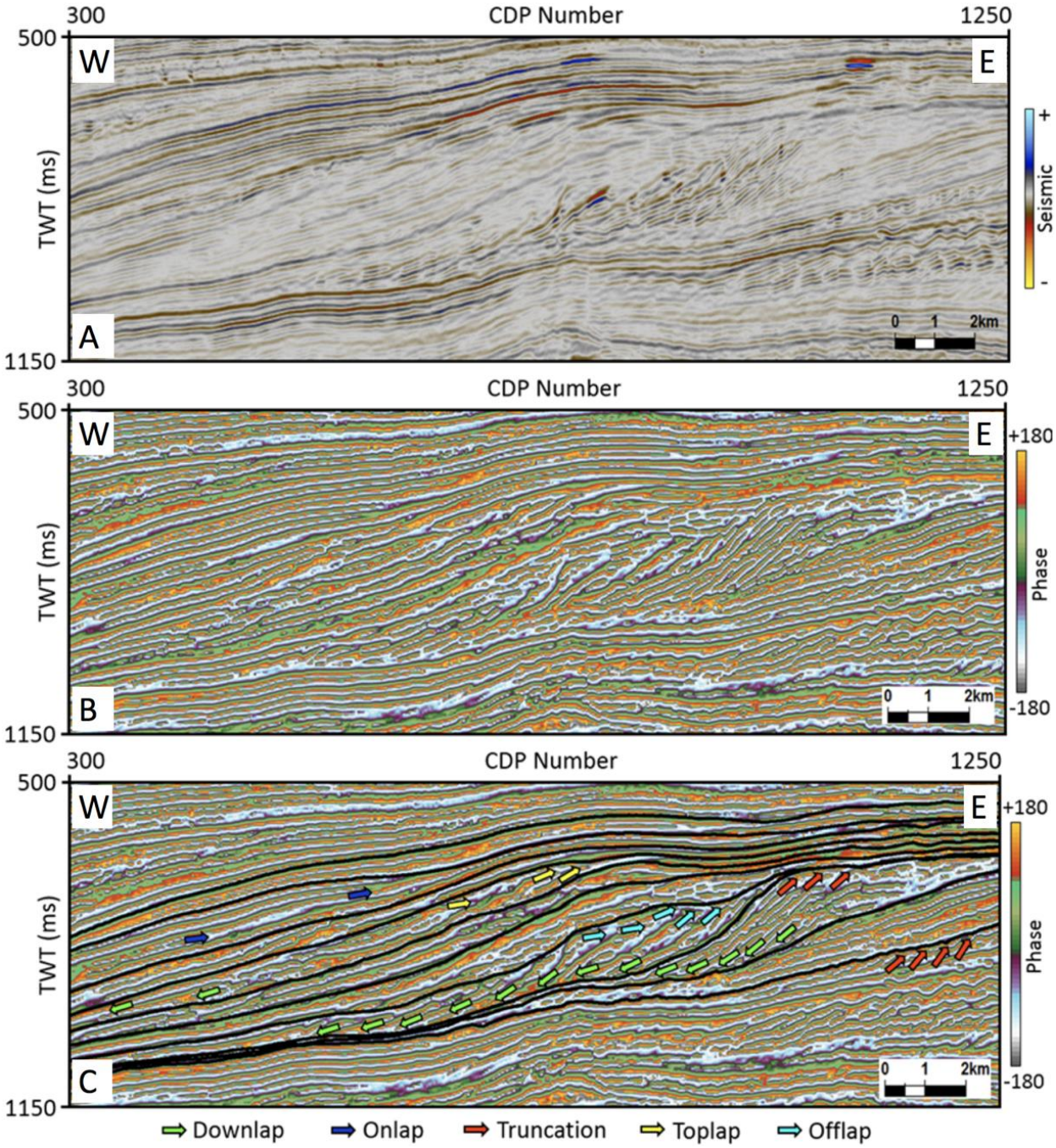

Figure 23. A representative inline seismic and corresponding instantaneous phase. (A) Seismic amplitude section, (B) instantaneous phase, and (C) instantaneous phase with interpreted sequence boundaries.

The MFS records the deepest water facies within a sequence and marks the turnaround from transgression to normal regression. The MFS is commonly associated with sediment condensation or starvation. The TST is overlain by the second package, which shows

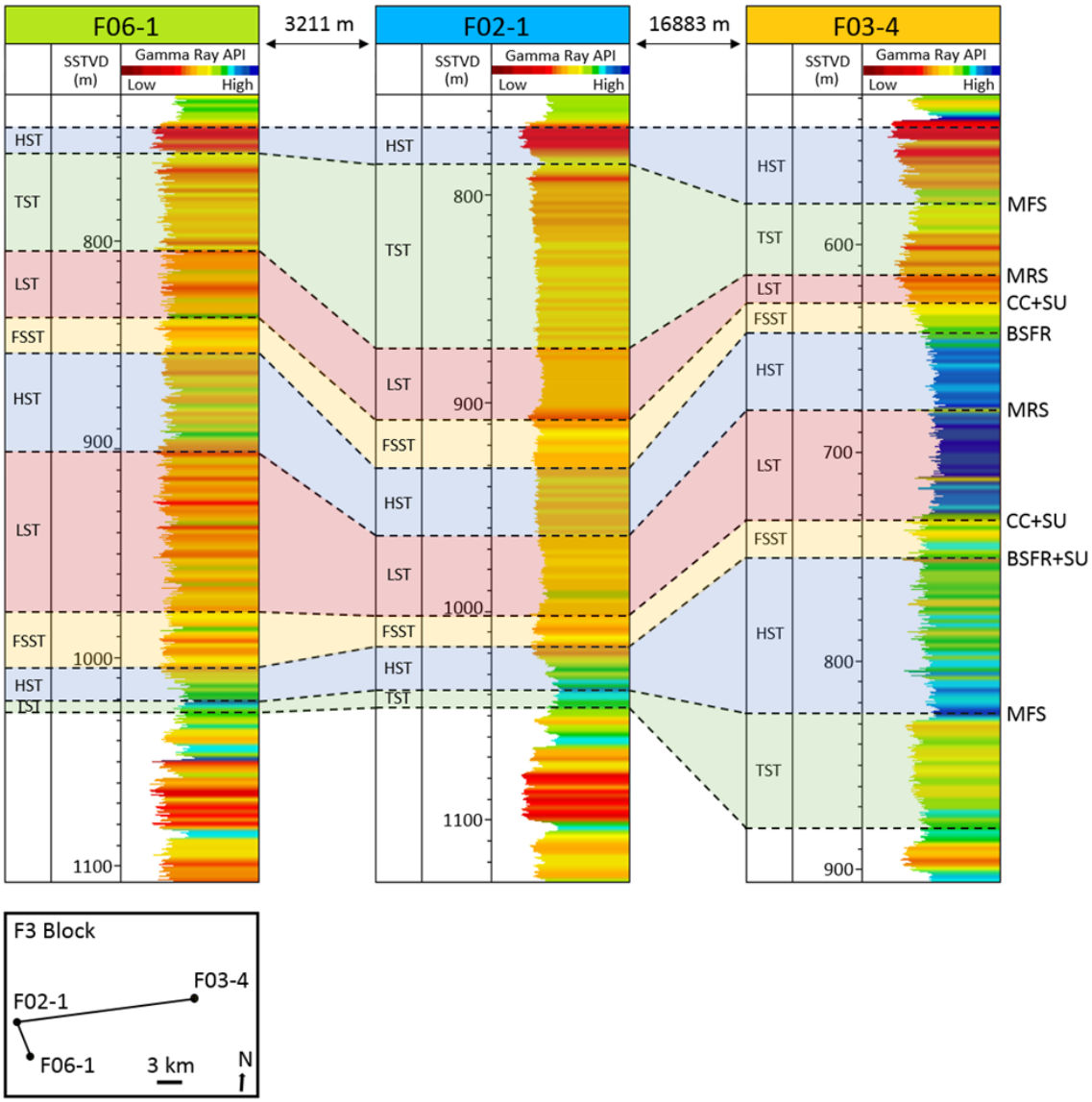

Figure 24. Cross well log correlation showing the systems tracts and major bounding surfaces interpretation. HST: highstand systems tract, TST: transgressive systems tract, LST: lowstand systems tract, FSST: falling stage systems tract, MFS: maximum flooding surface, MRS: maximum regressive surface, CC: correlative conformity, SU: subaerial unconformity, BSFR: basal surface of forced regression, SSTVD: subsea total vertical depth.

prograding parasequence sets. This package shows dipping and prograding sigmoidal reflections that downlap onto the MFS (or downlapping surface; Figure 23). Thus, this package is interpreted as an HST which is landward restricted and contains normal regression deposits. Well logs for this interval are characterized by upward decreasing GR values. The package is bounded at the bottom by the MFS and at the top by both the subaerial unconformity (SU) and the basal surface of forced regression (BSFR). The SU is interpreted to be the result of both regional uplift and local uplift caused by Zechstein salt intrusion into the overlying sediments. The third package is characterized by offlap reflection terminations of a set of prograding clinoforms. This unit is confined to the basinward direction indicating a detached forced regressive unit (Figure 23). Therefore, this interval is interpreted as a falling stage systems tract. The FSST is bounded at the bottom by the BSFR and at the top by the SU and correlative conformity (CC). The CC corresponds to the end of forced regression. The BSFR corresponds to the seafloor at the onset of forced regression (De Bruin and Bouanga, 2007). The surface bounding the FSST at the top is interpreted as the first sequence boundary (SB). The FSST interval cannot be clearly identified in well logs; its interpretation is thus solely based on seismic geometries.

Sequence 2 comprises normal regressive units (LST, HST, and FSST). LST shows a rise in base level after the earlier fall, and it overlies the FSST of Sequence 1 (Quayyum et al., 2013; Figure 25). In all three wells, LST deposits are characterized by overall blocky log patterns with low GR values. LST is separated from the overlain HST by a distinct maximum regressive surface, MRS (or transgressive surface, TS). Note the Sequence 2 does not include a TST between the LST and HST. This is because the TST is very thin and cannot be fully resolved at seismic resolution. In all three wells, there is no clear evidence indicating the TST and associated MFS. The HST of Sequence 2 contains previous topsets of the HST of Sequence 1 and is

bounded at the top by the BSFR. In Well F03-4, the units are characterized by an upward decreasing pattern, while the geometry is questionable in basinward Wells F02-1 and F06-1. The above unit is interpreted as a second falling stage within the target interval; therefore, the corresponding unit is interpreted as a FSST. The top of the FSST (CC+SU) is interpreted as the second SB marking the end of Sequence 2 (Figure 25).

Sequence 3 starts with a regressive system interpreted as the second lowstand systems tracts (Figure 25). The LST interval is characterized by a blocky GR response in Wells F02-1 and F06-1, whereas it shows an upward decreasing pattern in Well F03-4. The LST is bounded at the top by the second transgressive surface (Figure 25). Onlap structures, which form after the deposition of the LST, indicate a relative rise in sea level. During this stage, the rate of creation of accommodation is faster than the rate of sediment accumulation. According to these observations, this interval is interpreted as the second transgressive systems tract, which is bounded at the top by a MFS (Figure 25). The above package is characterized by upward decreasing GR values, while its geometry remains questionable in seismic sections (Figure 25). Therefore, this unit is interpreted as the third highstand systems tract comprising aggrading normal regressive deposits with relatively low sedimentation rate. A complete systems tracts interpretation is shown by Figures 25, 26, and 27.

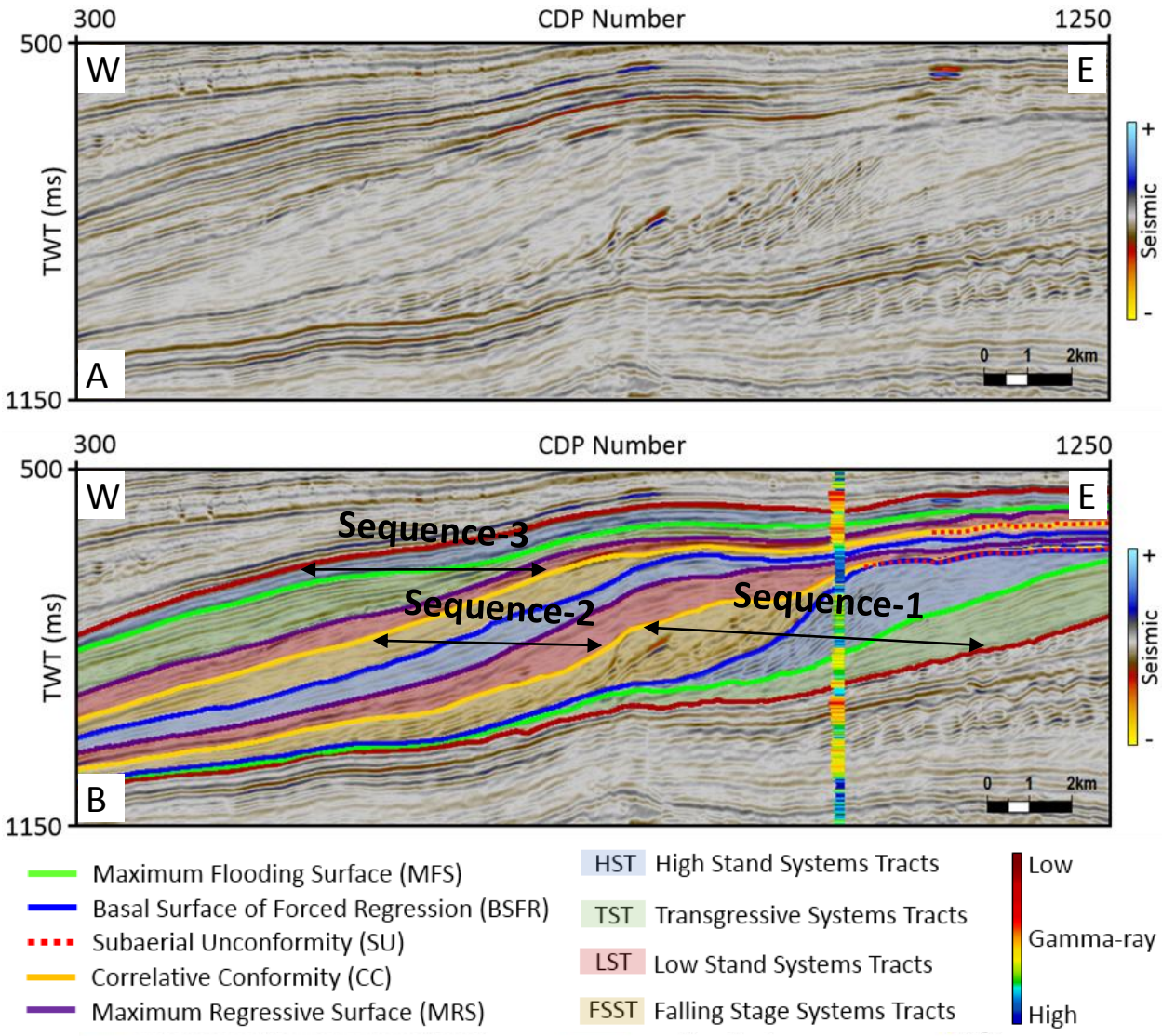

Figure 25. Systems tracts interpretation (Well F03-4). (A) Uninterpreted seismic section, (B) interpreted systems tracts overlaid on seismic. Well F03-4 displays GR log.

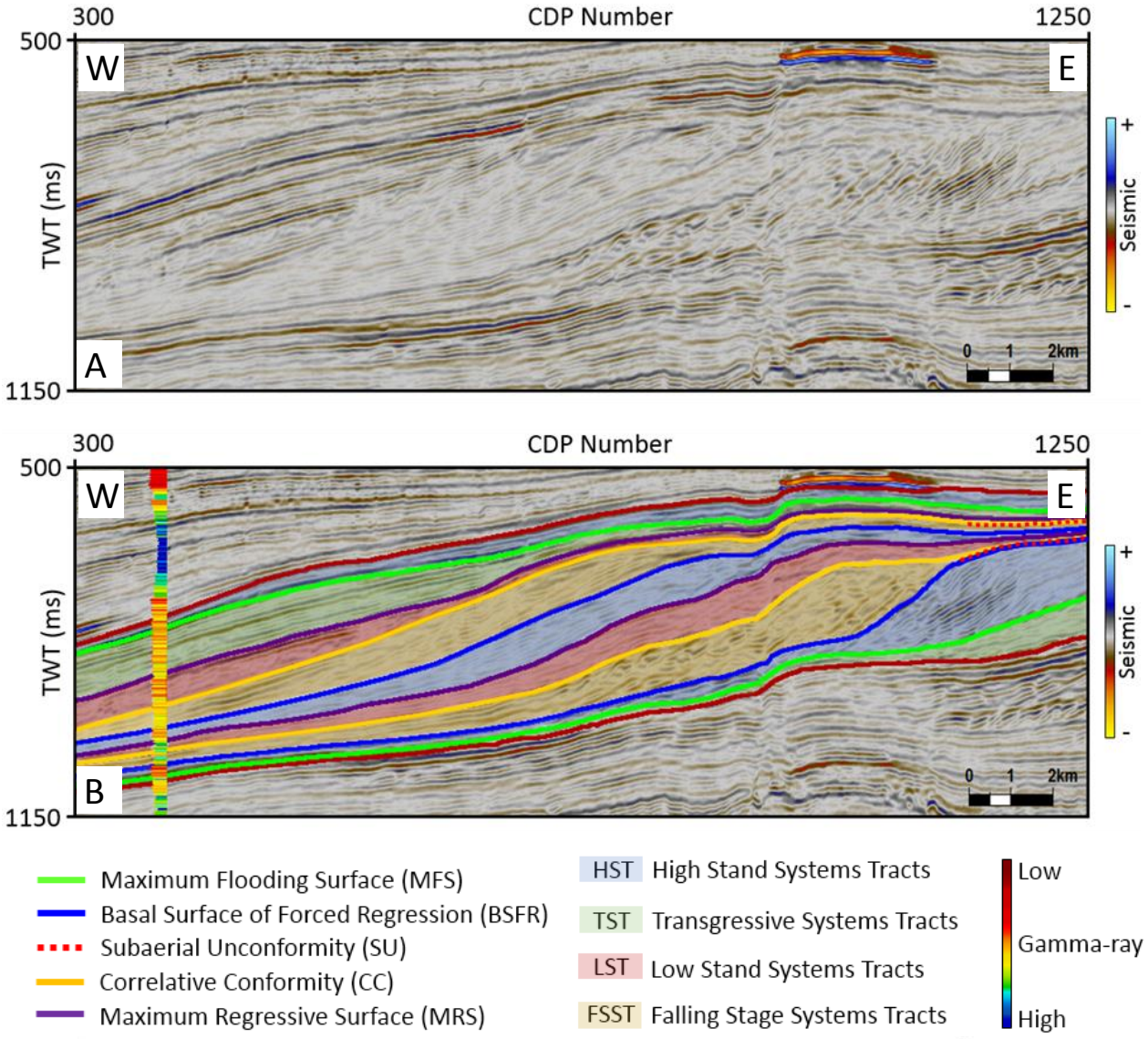

Figure 26. Systems tracts interpretation (Well F02-1). (A) Uninterpreted seismic section, (B) interpreted systems tracts overlaid on seismic. Well F02-1 displays GR log.

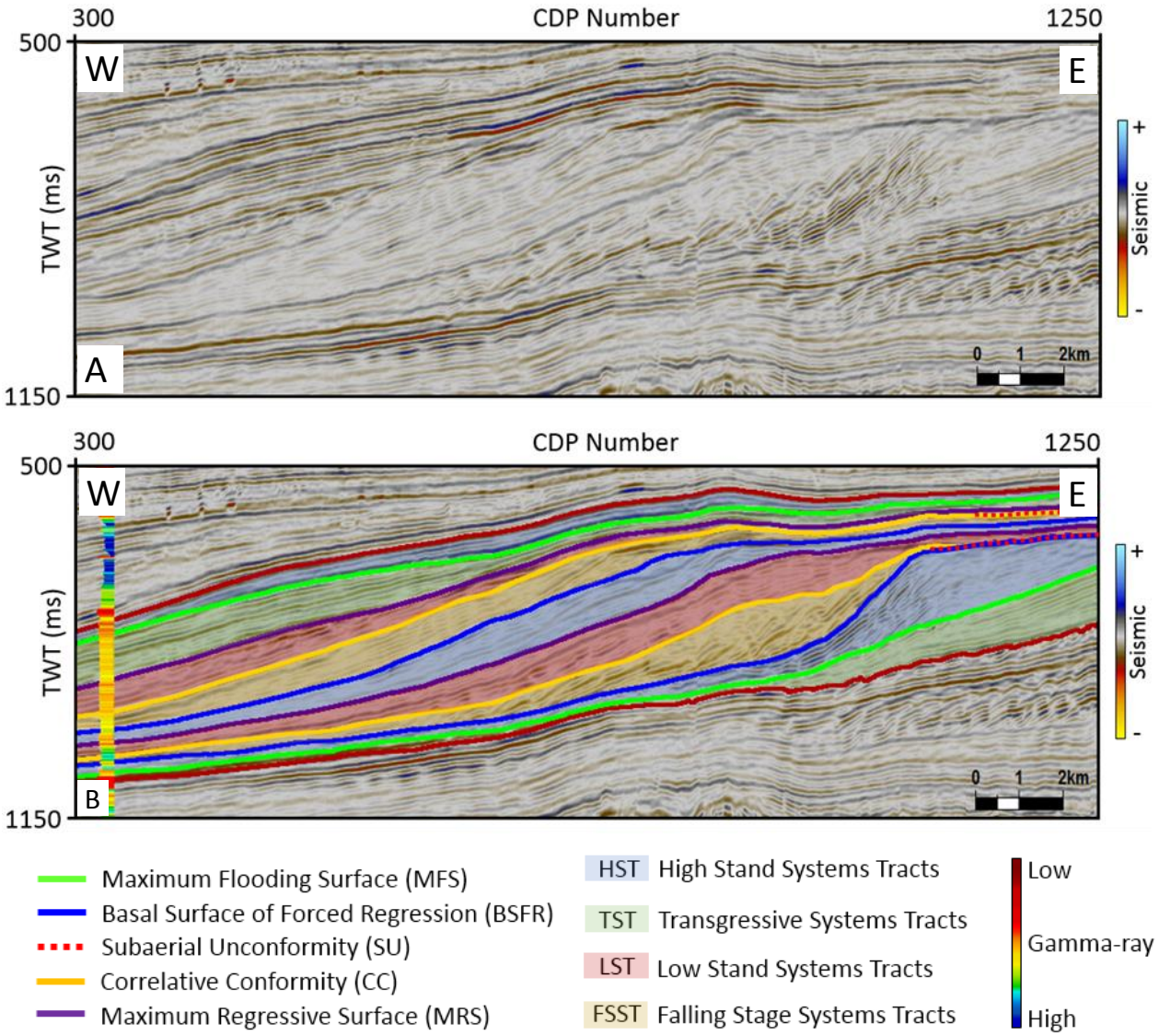

Figure 27. Systems tracts interpretation (Well F06-1). (A) Uninterpreted seismic section, (B) interpreted systems tracts overlaid on seismic. Well F06-1 displays GR log.

4. SURFACE ESTIMATION

In previous sections, I have discussed seismic sequence analysis derived from the interpretation of selected seismic sections. This section discusses how the identified sequence bounding surfaces can be semi-automatically propagated over the entire 3D seismic volume by using multiple seismic attributes. The section starts with an introduction of the Dijkstra's shortest path algorithm (Dijkstra, 1959), which is used for the semi-automatic horizons picking. Then I illustrate the workflow of semi-automatic horizon picking and apply it to the F3 seismic survey.

4.1 Dijkstra's Shortest Path Algorithm

The objective of Dijkstra's algorithm is to find the shortest path between any vertexes in a weighted graph. Below, I summarize the principles behind the algorithm through an example problem (Figure 28-A). For more details, please refer to the original paper (Dijkstra, 1959).

In the given graph, the objective is to find the shortest weighted path from the initial Vertex A to the target Vertex C. The shortest path between two given vertexes is the path that has the smallest summarized distance among all the candidate paths. The algorithm starts assigning a tentative shortest distance value from Vertex A to all vertexes in the graph. This value is zero for the initial Vertex A to Vertex A, and infinity for Vertex A to all other vertexes since they are initially unknown (Figure 28-B). These values are only updated if the distance from the previous vertex is less than its current value. The algorithm starts by visiting the unvisited neighbors of the Vertex A, which are Vertexes D and B (Figure 28-C). For the current Vertex (A), the distance of each neighbor is summarized from the start vertex. The distance from Vertex A to Vertex B and Vertex A to Vertex D is 6 and 1, respectively. If the calculated

distance of a vertex is smaller than the known distance, the algorithm updates the shortest distance. Therefore, distances of Vertexes B and D are updated to 6 and 1, respectively. Vertex A is added to the list of visited vertexes, and it is not visited again. Since Vertex D has the shortest path to Vertex A, then the current start point becomes Vertex D. Now the algorithm begins to compare the distance between Vertex D and its neighborhood Vertexes B and E (Figure 28-D). The algorithm repeats the same steps for all vertexes in the graph and finds the shortest path from Vertex A to Vertex C is seven via Vertexes D and E. The following section discusses the application of this algorithm to semi-automatic horizon picking.

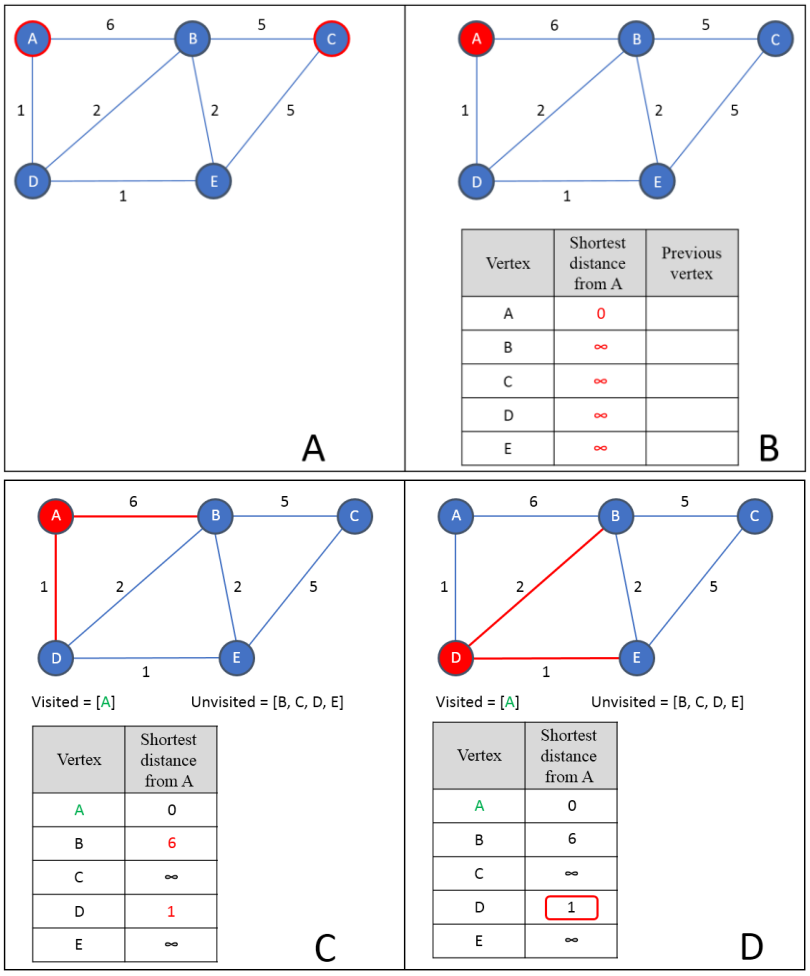

Figure 28. Cartoon showing an example of application of Dijkstra's shortest path algorithm (Inferred from Dijkstra, 1959).

4.2 Semi-automatic Surface Tracking

This section discusses how to use multiple seismic attributes to track picked horizons semi-automatically. The input seismic data and attribute volumes have the same geometries consisting of 501 inline, and 951 crossline sections (Figure 29). The algorithm requires three groups of input data: seismic data volume, seismic attribute volumes, and sequence bounding surfaces interpreted from selected seismic lines. The input seismic attributes include inverted P-impedance and porosity volumes. Manually picked sequence boundaries on selected inlines (100, 200, 300, 400, 500, 600) function as the seeds for the semi-automatic sequence boundaries tracking. Another input is the interpolated sequence boundaries based on the selected lines

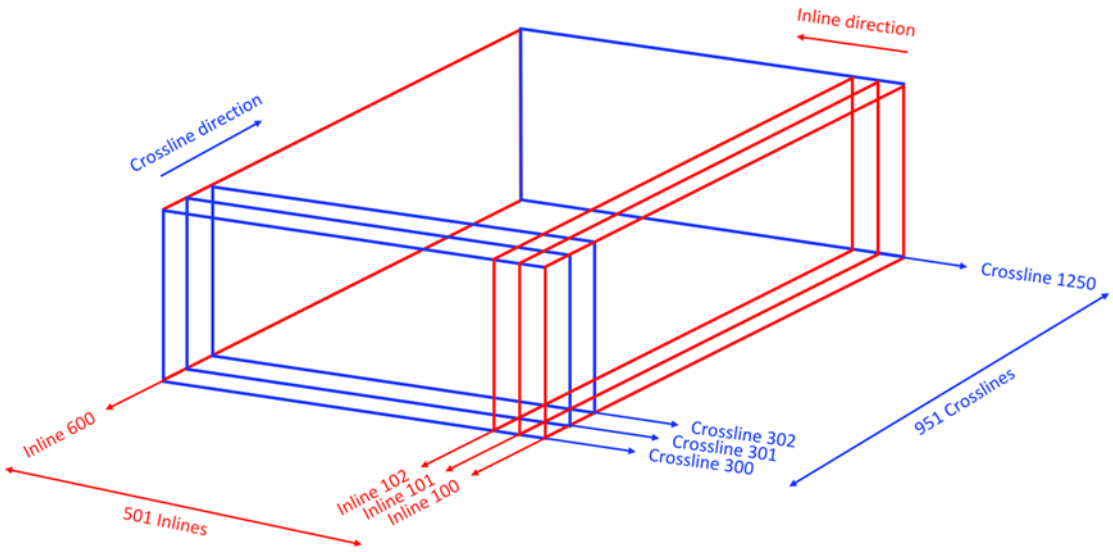

Figure 29. Cartoon showing input seismic attributes' geometry.

using Petrel software (Figure 30). The interpolated sequence boundaries function as the center of the searching window for the automatic horizon picking. Figure 31 shows the strategy for defining the searching window. The tracking direction is the crossline direction. Trace 1 and Trace 501 correspond to inlines 100 and 600 (key seismic lines), respectively. The black curve in

Figure 31 is the initial interpolated surface, and it functions as the center of the searching time window. The red samples centered on the black curve represent the vertical searching window.

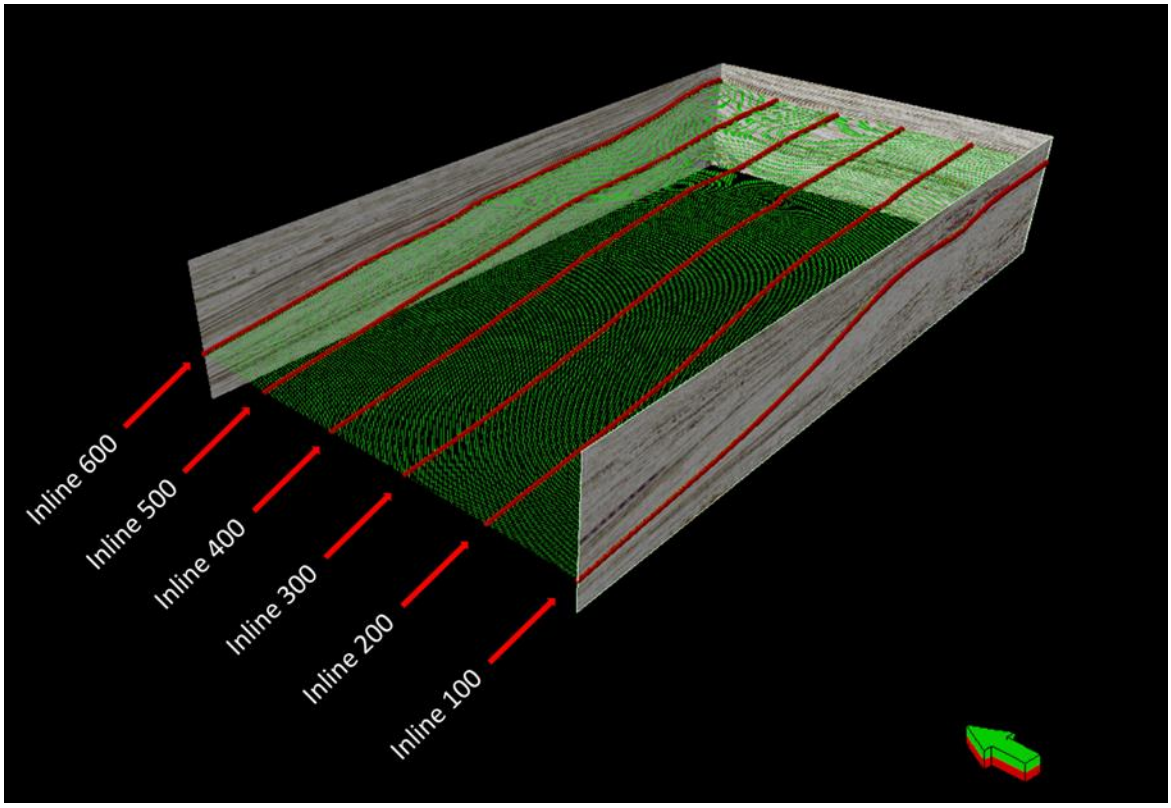

Figure 30. An example interpolated surface (green) based on the interpretation on limited lines (red lines).

The Dijkstra's algorithm searches for the shortest path between user-defined points. The manual interpretation on the key lines functions as the defined points. Each sample within the search window functions as the candidate passing vertex for the shortest path. I define distance between neighboring traces as:

$$d(i, j, m, n) = 2 - amp\_sim[tra(i, j, m), tra(i, j + 1, n)] - por\_sim[tra(i, j, m), tra(i, j +1, n)] \quad (10)$$

Where i, j are the inline and crossline number, m or n is the time index for the trace (i, j) and $amp\_sim[tra(i, j, m), tra(i, j +1, n)]$ is the similarity between the waveform centered at time

index *m* of trace (*i*, *j*) and the waveform centered at the time index *n* of trace (*i*, *j*+1). Similarly, *por_sim[tra(i, j, m), tra(i, j +1, n)]* is the similarity between the porosity centered at time index *m* of trace (*i*, *j*) and the porosity centered at the time index *n* of trace (*i*, *j*+1). The resulting surface is the cyan curve in Figure 31. In this study, a length of 11-sample window is used to compute the similarity (Figure 32).

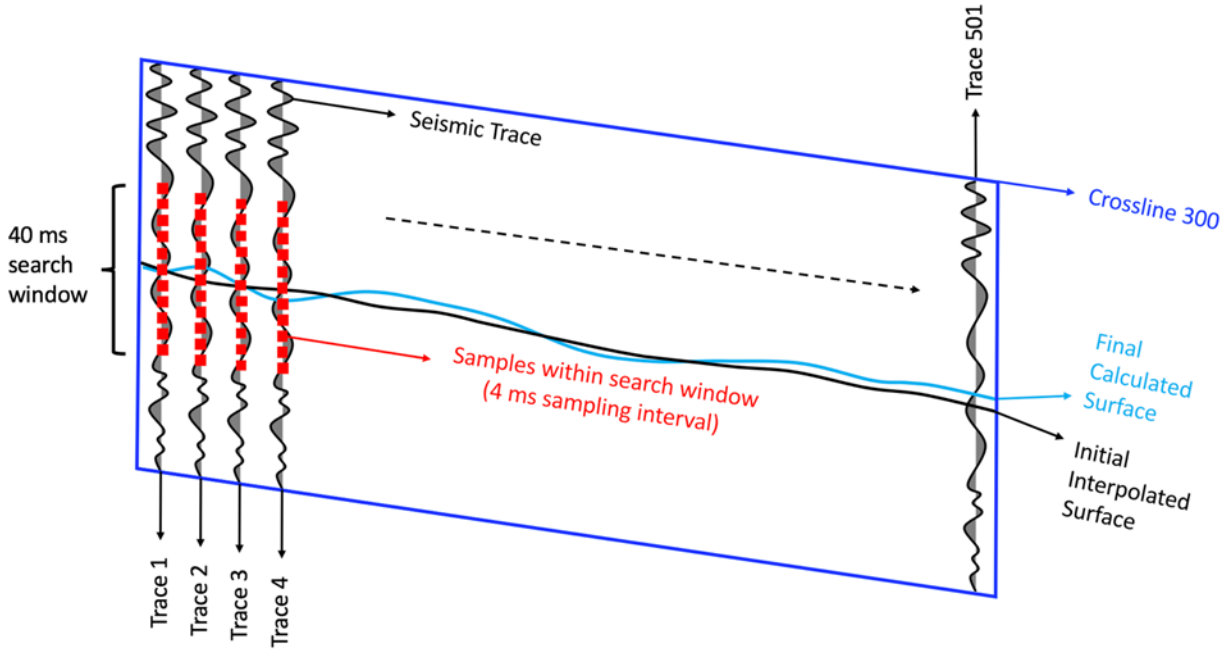

Figure 31. Cartoon showing the strategy of computing the similarity of two waveform.

Selecting the proper seismic attributes is the key to successful horizon tracking using the proposed workflow. Figure 33 shows tracked horizons overlaid on an inline seismic section. The horizons were determined using waveform, acoustic impedance, porosity, inline and crossline dips volumes. Figure 34 shows the tracked horizons computed from waveform, acoustic impedance, and porosity volumes. Note that there are "discontinuities" for tracked horizons when the inline and crossline dips attributes are included. This phenomenon is due to the fact

that we cannot obtain an accurate dip estimation for all the samples within the seismic survey. In this research, I use seismic waveform, acoustic impedance, and porosity volumes to track the horizons over the whole seismic survey. Figure 34 shows a zoomed comparison between the initial interpolated surfaces and the semi-automatically calculated surfaces. Note that the initial surfaces are crossing seismic reflection events, while the new semi-automatically calculated surfaces successfully follow the same seismic phase. Figure 35 shows the tracked horizons overlaid on an inline seismic section. Figures 36 shows an example sequence boundary surface in 3D view that is semi-automatically calculated by using this algorithm.

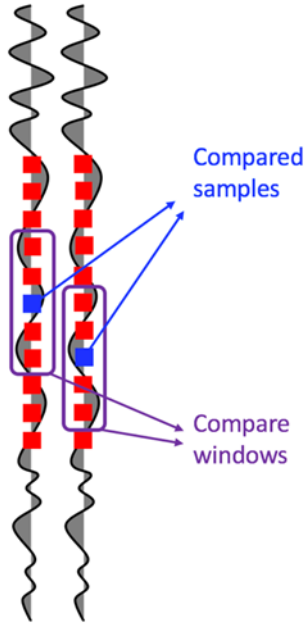

Figure 32. Cartoon showing the strategy of waveform comparison window.

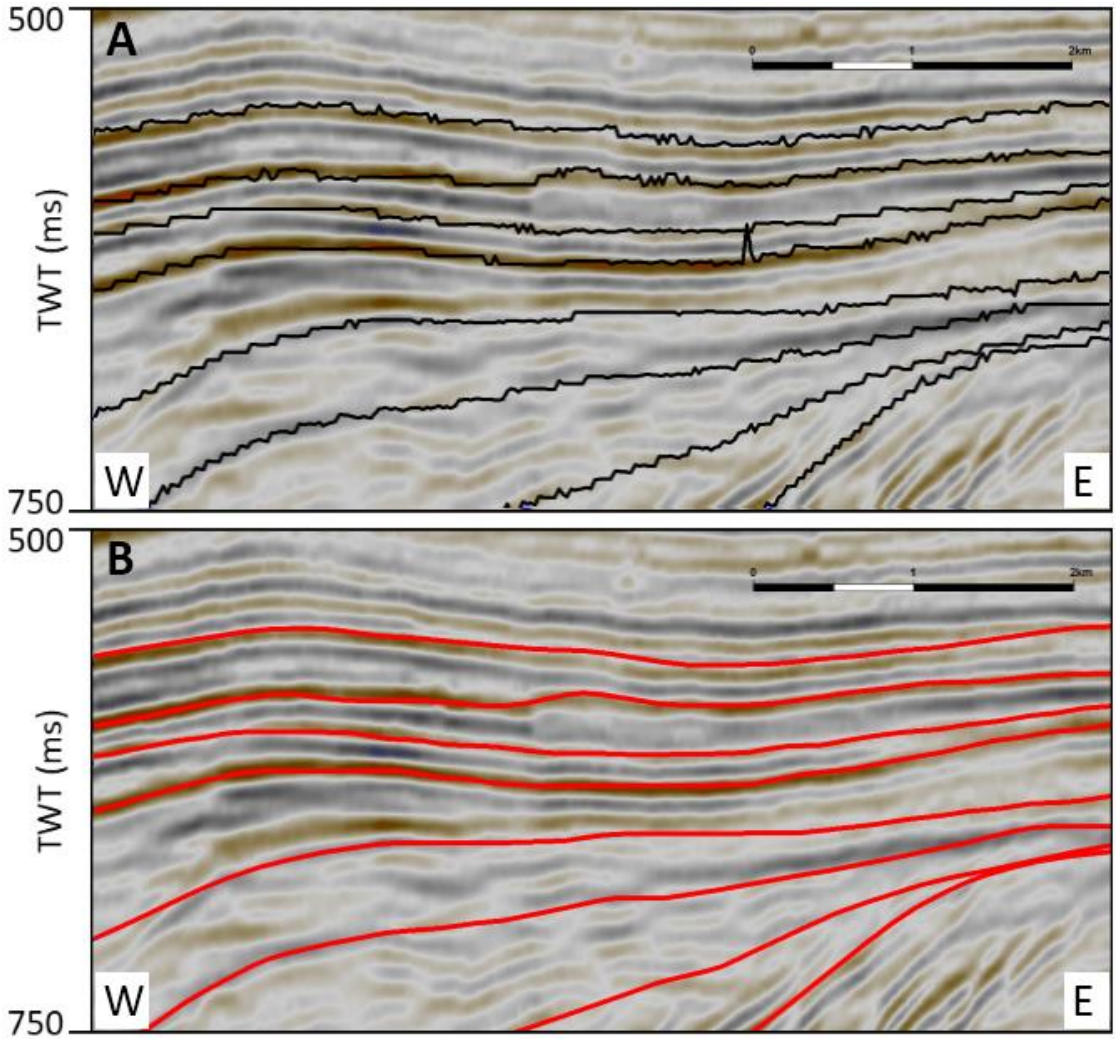

Figure 33. A zoomed comparison of calculated surfaces using different seismic attributes. (A) The tracked horizons using seismic waveform, porosity, acoustic impedance, inline and crossline dips attributes; (B) the tracked horizons using seismic waveform, porosity, and acoustic impedance attributes.

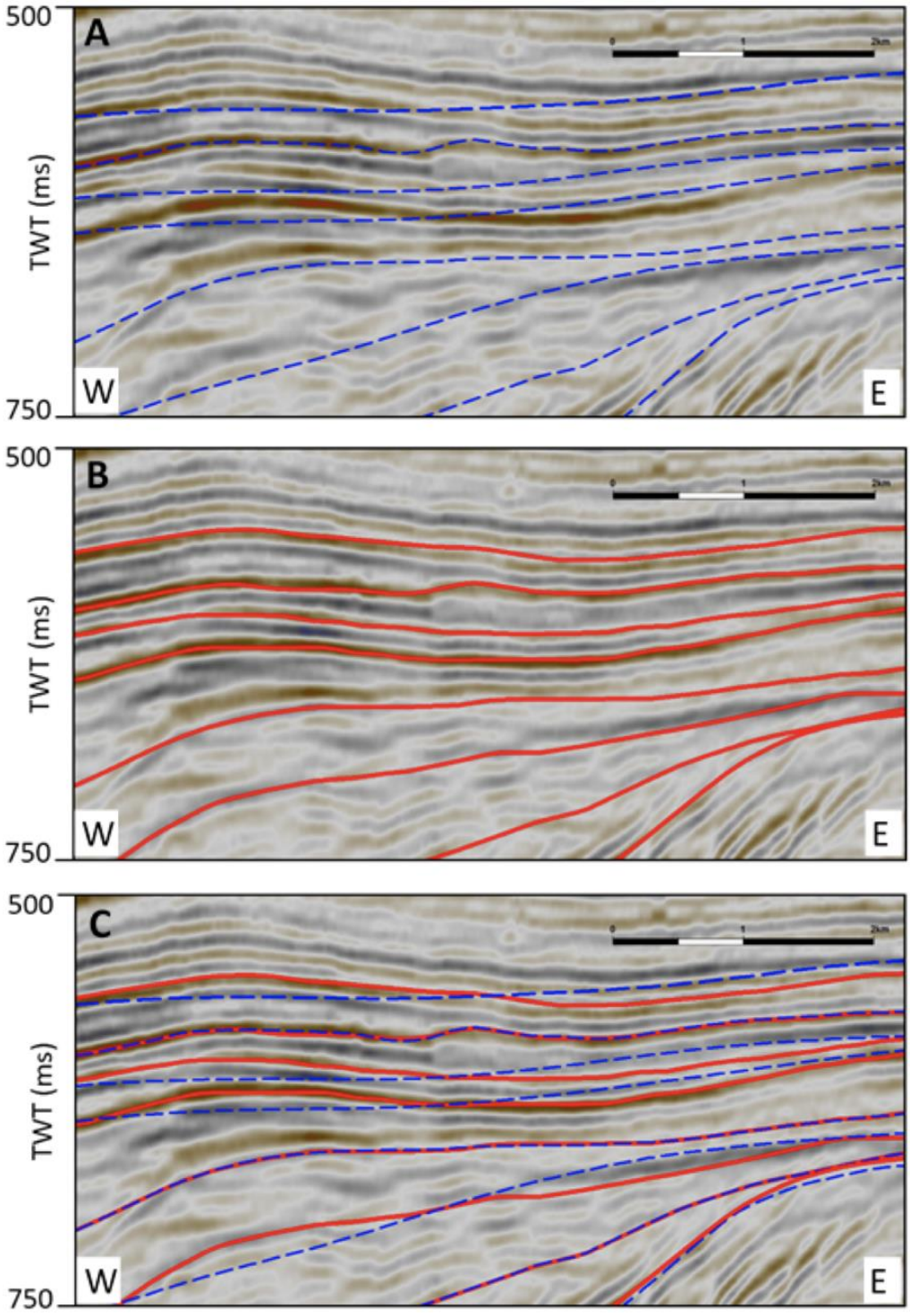

Figure 34. A zoomed comparison of (A) initial interpolated surfaces, (B) semi-automatically calculated surfaces, and (C) interpolated and calculated surfaces together.

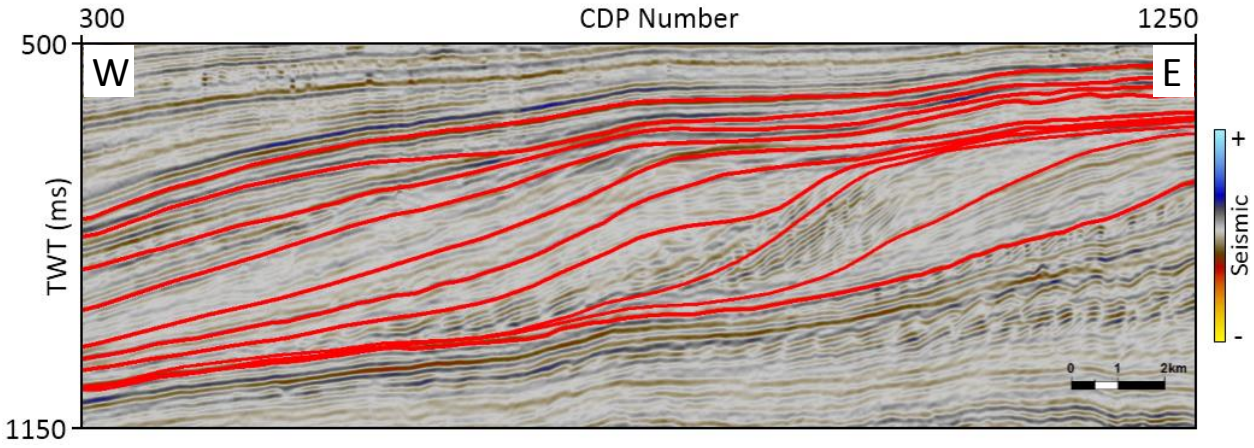

Figure 35. Semi-automatically calculated sequence bounding surfaces overlaid on inline seismic section.

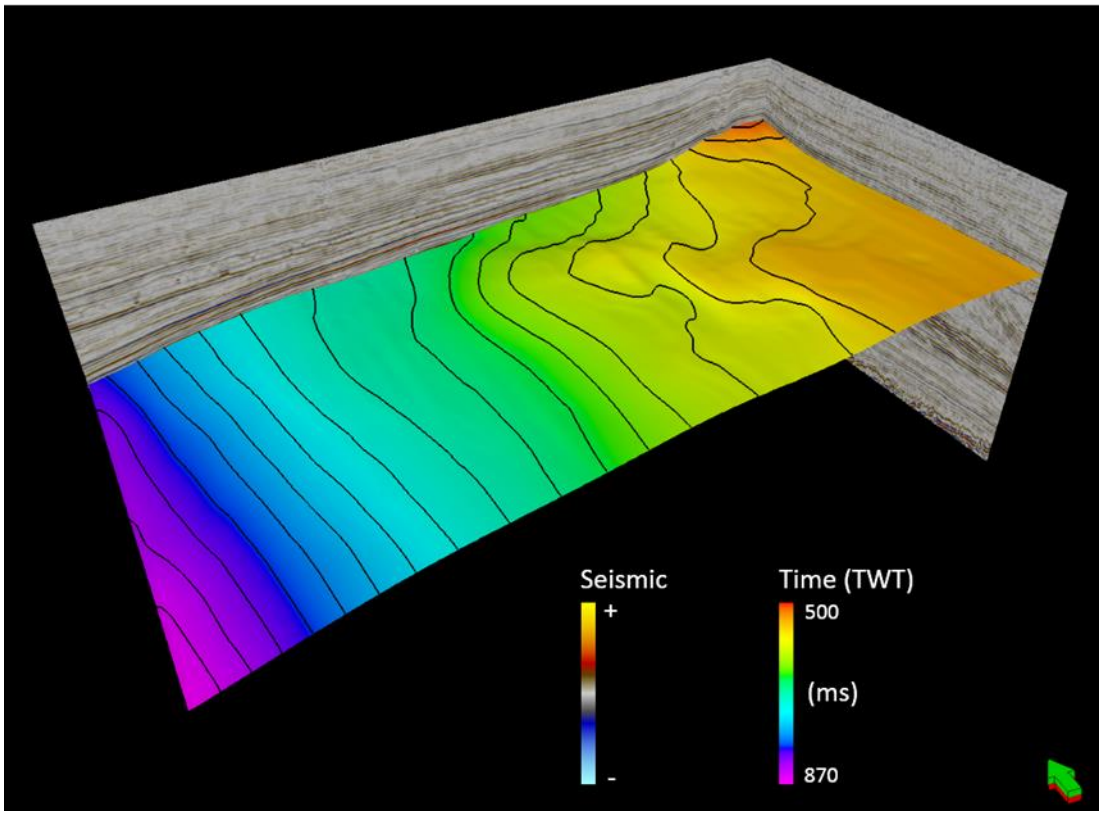

Figure 36. An example of a semi-automatically calculated sequence bounding surface.

5. DISCUSSIONS

Manual horizon interpretation is one of the most time-consuming tasks in seismic interpretation. The process is performed on 2D seismic sections individually and it may take several weeks or months to interpret all the interested horizons. The algorithm developed in this study significantly reduced the horizon interpretation time without reducing the accuracy of interpreted horizons.

Selecting the proper seismic attributes is the key to successfully implementing the workflow developed in this research. In my application, the most suitable attributes set were seismic waveform, acoustic impedance, and porosity volumes. The inline and crossline dip attributes introduced "discontinuities" in the tracked horizons. Therefore, I suggest excluding dip attributes in the automatic horizons tracking when there is low confidence about the dip estimation. Considering that the impedance is a direct function of the elastic parameter of the formation, I suggest including the impedance attribute in the automatic horizon tracking.

In my application, I need an average of 0.5 minutes to pick one horizon on one inline/crossline section. Thus, I need around 0.5*51*96=2448 minutes to interpret one horizon on the grid of ten by ten (I picked the horizons every ten inlines and ten crosslines.) The tested seismic survey has 501 inlines and 951 crosslines.) I spent around 24480 minutes to identify ten horizons needed to construct the systems tracts in my application.

The time of the new workflow includes following parts: (1) manual interpretation on selected sections, (2) seismic attributes computation, and (3) semi-automatic horizon tracking.

I need 0.5*6=3 minutes to interpret one horizon on the selected sections. I spent two days (24*60*2=2880 minutes) to compute the acoustic impedance and porosity attributes. The algorithm was implemented using Matlab and needed around 1500 minutes to track ten horizons on a Microsoft-based operating system (2.30 GHz, 2 processors). This computation time can be greatly reduced if we implement the algorithm on clusters through Message Passing Interface (MPI) technology. In this case, the rough total time is 3*10+2880+1500=4410 minutes (equals to 73.5 hours) which is much smaller than 24480 minutes (equals to 408 hours) required for manual horizons picking.

I noticed an interbedded high-low impedance pattern indicated by the white arrows in Figure 14. Unfortunately, I could not find any related literature about this pattern. However, I suspect that salt activities may be responsible for such high-low impedance pattern.

6. CONCLUSIONS

In this study, I developed a new algorithm to track sequence bounding surfaces semi-automatically. The algorithm used seismic attributes and manually interpreted sequence boundaries to propagate the manual interpretation to whole survey. The attributes used in this study are the P-impedance, porosity, and seismic waveform. The manual sequence stratigraphic interpretation of user selected inlines function as the control for the semi-automatic horizon picking. To test the effectiveness of the algorithm, the workflow was applied to a 3D seismic volume acquired in Dutch sector (F3 Block) of the southern North Sea Basin. The target zone of this study is basinward prograding units of the Eridanos delta. The application proved that the new picking algorithm can significantly reduce the total interpretation time in the practice of sequence bounding surface identification. The accuracy of the computed attributes (P-impedance and porosity) directly affect the quality of picked horizons. The attribute combination used in this study does not necessarily have to fit any data in every case. The selected seismic attributes may vary case by case depending on the quality of input seismic data. The users should compare seismic attributes changes near the sequence boundaries and determine which attributes are the optimum attributes for semi-automatic horizon picking.

REFERENCES

Amosu, A., and Y. Sun, 2017, WheelerLab: An interactive program for sequence stratigraphic analysis of seismic sections, outcrops and well sections and the generation of chronostratigraphic sections and dynamic chronostratigraphic sections: SoftwareX, 6, 19-24.

Barnes, A. E., 2000, Attributes for automating seismic facies analysis: SEG, Expanded Abstracts, 553-556.

Barrash, W., and E. C. Reboulet, 2004, Significance of porosity for stratigraphy and textural composition in subsurface, coarse fluvial deposits: Boise Hydrogeophysical Research Site, GSA Bulletin, 116, 1059-1073.

Bijlsma, S., 1981, Fluvial sedimentation from the Fennoscandian area into the north-west European Basin during the Late Cenozoic: Geologie en Mijnbouw, 60, 337-345.

Borůvka, O., 1926, On a certain minimal problem: Praca Moravske Prirodovedecke Spolecnosti, 3, 37–58.

Cameron, T. D. J., A. Crosby, P. S. Balson, D. H. Jeffery, G. K. Lott, J. Bulat, and D. J. Harrison, 1992, The geology of the southern North Sea: British Geological Survey, United Kingdom Offshore Regional Report.

Cameron, D., D. Van Doorn, C. Laban, and H. J. Streif, 1993, Geology of the southern North Sea basin: ASCE.

Catuneanu, O., 2006, Principles of sequence stratigraphy: Elsevier.

Chatterjee, S., M. Burreson, B. Six, and J. M. Michel, 2016, Seismically Derived Porosity Prediction for Field Development-An Onshore Abu Dhabi Jurassic Carbonate Reservoir Case Study: SPE, Abu Dhabi International Petroleum Exhibition & Conference.

Contreras, A. J., and R. B. Latimer, 2010, Acoustic impedance as a sequence stratigraphic tool in structurally complex deepwater settings: The Leading Edge, 29, 1072-1082.

Cooke, D. A., and W. A. Schneider, 1983, Generalized linear inversion of reflection seismic data: Geophysics, 48, 665-676.

De Bruin, G., and E. C. Bouanga, 2007, Time attributes of stratigraphic surfaces, analyzed in the structural and wheeler transformed domain: SPE, EAGE, 69th EAGE Conference & Exhibition incorporating SPE EUROPEC.

Dijkstra, E. W., 1959, A note on two problems in connexion with graphs: Numerische Mathematik, 1, 269-271.

Doppert, J. W. C., G. H. J. Ruegg, C. J. Van Staalduinen, W. H. Zagwijn, and J. G. Zandstra, 1975, Formaties van het Kwartair en Boven-Tertiar in Nederland, in Zagwin, W. H., and C. J. Van Staalduinen: Toelichting bij geologische overzichtkaarten van Nederland: National Geological Service, Haarlem, 11-56.

Draper, N. R., and H. Smith, 1966, Applied regression analysis: John Wiley & Sons Inc.

Faraklioti, M., and M. Petrou, 2004, Horizon picking in 3D seismic data volumes: Machine Vision and Applications, 15, 216-219.

Geluk, M., 2017, Permian in geology of the Netherlands: Geology of the Netherlands, 63-83.

Glennie, K. W., and P. L. E. Boegner, 1981, Sole pit inversion tectonics: Petroleum geology of the continental shelf of North-West Europe: Institute of Petroleum, 110-120.

Glennie, K. W., 1986, Development of NW Europe's Southern Permian gas basin: Geological Society, London, Special Publications, 23, 3-22.

Glennie, K. W., (Ed.), 2009, Petroleum geology of the North Sea: basic concepts and recent advances: John Wiley & Sons Inc.

Gutiérrez, M. A., 2001, Rock physics and 3D seismic characterization of reservoir heterogeneities to improve recovery efficiency: Ph.D. thesis, Stanford University.

Hampson, D., T. Todorov, and B. Russell, 2000, Using multi-attribute transforms to predict log properties from seismic data: Exploration Geophysics, 3, 481-487.

Hampson, D. P., J. S. Schuelke, and J. A. Quirein, 2001, Use of multiattribute transforms to predict log properties from seismic data: Geophysics, 66, 220-236.

Harding, R., and M. Huuse, 2015, Salt on the move: Multi stage evolution of salt diapirs in the Netherlands North Sea: Marine and Petroleum Geology, 61, 39-55.

Henry, S. G., 1997, Catch the (seismic) wavelet: AAPG Explorer, 18, 36-38.

Hou, Q., Zhu, J., and Lin, B., 2016, Estimation of reservoir porosity using probabilistic neural network and seismic attributes: Global Geology, 19, 6-12.

Hunt, D., and M. E. Tucker, 1992, Stranded parasequences and the forced regressive wedge system tract: Deposition during base-level fall: Sedimentary Geology, 81, 1-9.

Hunt, D., and M. E. Tucker, 1995, Stranded parasequences and the forced regressive wedge system tract: Deposition during base-level fall, Reply: Sedimentary Geology, 95, 147160.

Kalkomey, C. T., 1997, Potential risks when using seismic attributes as predictors of reservoir properties: The Leading Edge, 16, 247-251.

Khalifa, M. K., and A. Alta'ee, 2011, An integrated petrophysical analysis to evaluate sequence stratigraphy of the Winduck Interval in the Neckarboo sub-basin, Darling Basin, NSW: SPE, Asia Pacific Oil and Gas Conference & Exhibition.

Krassay, A. A., 1998, Outcrop and drill core gamma-ray logging integrated with sequence stratigraphy: examples from Proterozoic sedimentary succession of northern Australia: AGSO journal of Australian Geology and Geophysics, 17, 285-300.

Latimer, R. B., R. Davidson, and P. Van Riel, 2000, An interpreter's guide to understanding and working with seismic-derived acoustic impedance data: The Leading Edge, 19, 242-256.

Lavergne, M., and C. Willm, 1977, Inversion of seismograms and pseudo velocity logs: Geophysical Prospecting, 25, 231-250.

Lidmar-Bergström, K., C. D. Ollier, and J. R. Sulebak, 2000, Landforms and uplift history of southern Norway: Global and Planetary Change, 24, 211-231.

Lindseth, R. O., 1979, Synthetic sonic logs-A process for stratigraphic interpretation: Geophysics, 44, 3-26.

Maroni, C. S., A. Quinquis, and S. Vinson, 2001, Horizon picking on subbottom profiles using multi resolution analysis: Digital Signal Processing, 11, 269-287.

Martins-Neto, M. A., and O. Catuneanu, 2010, Rift sequence stratigraphy: Marine and Petroleum Geology, 27, 247-253.

Maurya, S. P., and P. Sarkar, 2016, Comparison of post stack seismic inversion method: A case study from Blackfoot Field, Canada: International Journal of Scientific and Engineering Research, 8, 1091-1101.

Miller, K. G., J. V. Browning, G. S. Mountain, M. A. Bassetti, D. Monteverde, M. E. Katz, J. Inwood, J. Lofi, and J. N. Proust, 2013, Sequence boundaries are impedance contrasts: Core-seismic-log integration of Oligocene-Miocene sequences, New Jersey shallow shelf: Geosphere, 9, 1257-1285.

Mitchum Jr, R. M., P. R. Vail, and S. Thompson III, 1977, Seismic stratigraphy and global changes of sea level: Part 2. The depositional sequence as a basic unit for stratigraphic analysis: Section 2. Application of seismic reflection configuration to stratigraphic interpretation: AAPG, 53-62.

Nance, R. D., G. Gutiérrez-Alonso, J. D. Keppie, U. Linnemann, J. B. Murphy, C. Quesada, R. A. Strachan, and N. H. Woodcock, 2012, A brief history of the Rheic Ocean: Geoscience Frontiers, 2, 125-135.

Nesetril, J., E. Milkova, and H. Nesetrilova, 2001, Otakar on minimum spanning tree problem: Translation of both the 1926 papers, comments, history: Discrete Mathematics, 233, 3-36.

Overeem, I., G. J. Weltje, C. Bishop-Kay, and S. B. Kroonenberg, 2001, The Late Cenozoic Eridanos delta system in the southern North Sea Basin: a climate signal in sediment supply?: Basin Research, 13, 293-312.

Qayyum, F., P. De Groot, and N. Hemstra, 2012, Using 3D Wheeler diagrams in seismic Interpretation-the HorizonCube method: First Break, 30, 103-109.

Qayyum, F., N. Hemstra, and S. Raman, 2013, A modern approach to build 3D sequence stratigraphic framework: Oil & Gas Journal, 111, 46-46.

Randen, T., B. Reymond, H. I. Sjulstad, and L. Sønneland, 1998, New seismic attributes for automated stratigraphic facies boundary detection: SEG, Expanded Abstracts, 628-631.

Riis, F., 1992, Dating and measuring of erosion, uplift and subsidence in Norway and the Norwegian shelf in glacial periods: Norwegian Journal of Geology, 72, 325-331.

Riis, F., 1996, Quantification of Cenozoic vertical movements of Scandinavia by correlation of morphological surfaces with offshore data: Global and Planetary Change, 12, 331-357.

Rohrman, M., P. Beek, P. Andriessen, and S. Cloetingh, 1995, Meso-Cenozoic morphotectonic evolution of southern Norway: Neogene domal uplift inferred from apatite fission track thermochronology: Tectonics, 14, 704-718.

Rohrman, M., P. Andriessen, and P. Beek, 1996, The relationship between basin and margin thermal evolution assessed by fission track thermochronology: an application to offshore southern Norway: Basin Research, 8, 45-63.

Russell, B., and Hampson, D., 1991, Comparison of post-stack seismic inversion methods: SEG, Expanded Abstracts, 876-878.

Russell, B. H., 1988, Introduction to seismic inversion methods: SEG.

Sales, J. K., 1992, Uplift and subsidence do northwestern Europe: possible causes and influence on hydrocarbon productivity: Norwegian Journal of Geology, 72, 253-258.

Schultz, P. S., S. Ronen, M. Hattori, and C. Corbett, 1994, Seismic-guided estimation of log properties: Part 1: A data-driven interpretation methodology: The Leading Edge, 13, 305-310.

Specht, D., 1990, Probabilistic neural networks: Neural Networks, 3, 109-118.

Taner, M. T., and R. E. Sheriff, 1977, Application of Amplitude, Frequency, and Other Attributes to Stratigraphic and Hydrocarbon Determination: Section 2: Application of seismic reflection configuration to stratigraphic interpretation: AAPG memoir, 26, 301-327.

Taner, M. T., F. Koehler, and R. E. Sheriff, 1979, Complex seismic trace analysis: Geophysics, 44, 1041-1063

Taner, M. T., J. S. Schuelke, R. O'Doherty, and E. Baysal, 1994, Seismic attributes revisited: SEG, Expanded Abstracts, 1104-1106.

Taner, M. T., 2001, Seismic attributes: Canadian Society of Exploration Geophysicists Recorder, 26, 48-56.

Tetyukhina, D., L. J. van Vliet, S. M. Luthi, and K. Wapenaar, 2010, High-resolution reservoir characterization by an acoustic impedance inversion of a Tertiary deltaic clinoform system in the North Sea: Geophysics, 75, 57-67.

Vail, P. R., 1987, Seismic stratigraphy interpretation using sequence stratigraphy: Part 1: Seismic stratigraphy interpretation procedure: AAPG, 1, 1-10.

Van Adrichem Boogaert, H. A., and W. F. P. Kouwe, 1993, Stratigraphic nomenclature of the Netherlands, revision and update by RGD and NOGEPA, Section A, General: Mededelingen Rijks Geologische Dienst, 50, 1-40.

Van Hoek, T., S. Gesbert, and J. Pickens, 2010, Geometric attributes for seismic stratigraphic interpretation: The Leading Edge, 29, 1056-1065.

Van Wagoner, J. C., D. Nummedal, C. R. Jones, D. R. Taylor, D. C. Jennette, and G. W. Riley, 1991, Sequence Stratigraphy Applications to Shelf Sandstone Reservoirs: Outcrop to Subsurface Examples: AAPG.

Walden, A. T., and R. E. White, 1998, Seismic wavelet estimation: a frequency domain solution to a geophysical noisy input-output problem: IEEE Transactions on Geoscience and Remote Sensing, 36, 287-297.

Wolak, J., N. Hemstra, J. Ochoa, and M. Pelissier, 2013, Reconstruction of depocenter evolution through time using relative stratigraphic thickness: The Leading Edge, 32, 172-177.

Wong, T. E., D. A. Batjes, and J. de Jager, 2007, Geology of the Netherlands: Edita-KNAW.

Wu, X., and D. Hale, 2015, 3D seismic image processing for unconformities: Geophysics, 80, 35-44.

Yu, Y., C. Kelley, and I. Mardanova, 2011, Automatic horizon picking in 3D seismic data using optical filters and minimum spanning tree (patent pending): SEG, Expanded Abstracts, 965-969.

Ziegler, P. A., 1975, The geological evolution of the North Sea area in the tectonic framework of North-Western Europe: Geological Survey of Norway, 316, 1-27.

Ziegler, P. A., 1977, Geology and hydrocarbon provinces of the North Sea: GeoJournal, 1, 7-32.